Experimental Evaluation of Microgrid Energy Management Using Surrogate-Assisted Optimization on PHIL and Smart-Grid Systems

Saiful Islam *, Sanaz Mostaghim, Michael Hartmann

Posted Date: 30 March 2026

doi: 10.20944/preprints202603.2378.v1

Keywords: multi-objective optimization; smart grid; renewable energy systems; surrogate-assisted optimization; decision-making; grid-forming; grid-following

Article

Experimental Evaluation of Microgrid Energy Management Using Surrogate-Assisted Optimization on PHIL and Smart-Grid Systems

Saiful Islam [1,2,*], Sanaz Mostaghim [1,3] and Michael Hartmann [2]

[1] Chair of Computational Intelligence, Faculty of Computer Science, Otto von Guericke University Magdeburg, Germany
[2] SRH University of Applied Sciences, School of Technology and Architecture (TEAC), Germany
[3] Fraunhofer Institute for Transportation and Infrastructure Systems IVI, Dresden, Germany
* Correspondence: saiful.islam@srh.de

Abstract

In this work, we present an integrated hybrid approach of multi-objective evolutionary decomposition algorithm for a microgrid-connected smart grid test-bench. The optimization technique was tested in a power hardware-in-the-loop setup, using different distributed energy resources. During evaluation, the optimization ran in real time. To reduce computational time, we added a surrogate-assistance to help find the feasible operational region and detect knee points for decision-oriented prioritization of candidate solutions. We focused more on human decision preferences instead of only choosing the best solution from the Pareto set, giving priority to decision-based knee points for dynamic constraints. The research integrates an OPAL-RT microgrid power hardware-in-the-loop platform with a Lucas-Nülle smart-grid laboratory system to investigate energy management system optimization under various operational modes. The proposed hybrid framework also incorporates a stochastic survival strategy to maintain both convergence and diversity of the search process. The method was evaluated in both grid-connected and off-grid modes, where the microgrid operates as the primary energy source for the smart-grid unit during off-grid mode. In off-grid operation, grid-forming objectives were applied, while grid-following objectives were used in grid-connected scenarios. In the grid-following mode, a selective physical replay mechanism was employed to reduce computational complexity while maintaining stable decision quality. In the results for grid-connected mode, it observed constrained feasible regions because of the limited renewable utilization and reliance on battery and grid support which shows the influence of measure system conditions. In the grid-forming scenario, the results reveal stable convergence behavior with consistent Pareto set quality across independent runs. Experimental validation demonstrates objective-dependent modeling capability for nonlinear system behavior such as battery stress, efficiently reduce thousands of candidate solutions to a small and robust Pareto set, and provide a practical decision-intelligence layer linking evolutionary optimization with real-time energy management systems.

Keywords: multi-objective optimization; smart grid; renewable energy systems; surrogate-assisted optimization; decision-making; grid-forming; grid-following

1. Introduction

An MG connects different energy resources and can operate either with the main grid or independently. Systems that work without the grid are called standalone or off-grid systems, while those connected to the grid are known as grid-connected or on-grid systems. Microgrids (MGs) face several challenges, and their main issues have been widely studied in recent years [1]. Research often focuses on technical, economic, and energy management system (EMS) problems. Recent studies pay special attention to technical topics like voltage-frequency (V-F) stabilization, total harmonic distortion (THD), and inverter voltage and frequency adjustment. Technical challenges also include

 doi:10.20944/preprints202603.2378.v1

load scheduling, adjusting for variable loads, and analyzing load profiles to meet demand. The supply from distributed energy resources (DERs) also plays a key role in balancing supply and demand in the MG system. The EMS issues are also equally important and one of the topic analyses and contributes in different literature in past years [2,3]. EMS issues like supply-demand balance, start and stop status of supply voltages and storage devices, equipment parameters are one of the top topics to discussed. Maximization of the renewable energy sources (RES) usage such as PV are also difficult in terms of maximum load and photovoltaic (PV) power variations.

MG systems face challenges in designing and sizing components such as PV panels, wind turbines (WT), diesel generators (DG), battery energy storage systems (BESS), and inverters for both grid-connected and off-grid setups [4]. Integrating with the utility grid is also difficult because it requires technical adjustments to these components [5]. The unpredictable nature of RES adds another layer of complexity, especially when connecting them to MGs. Other technical issues include limiting fault current in droop or V-F control for grid-tied inverters, finding the best microgrid configuration, ensuring reliable energy supply, managing DC link and input voltages, and achieving maximum power point (MPP) control in converters [5,6]. From a planning perspective, economic factors such as minimizing costs at peak load, balancing supply and demand, return on investment (ROI), internal rate of return (IRR), reducing the levelized cost of electricity (LCOE), as well as managing operational and maintenance costs (OPEX), net present cost (NPC), and capital expenditure (CAPEX) are all important in MG projects.

Multi-objective optimization (MOO) techniques are widely used, and specific algorithms of them are commonly applied to solve issues in MG systems [7,8]. MOO is one such technique that can be set up as either a maximization or a minimization problem. These algorithms use a population-based approach [9], where multiple solutions are considered in each iteration, and a new set of solutions is generated each time [10]. These techniques [10,11] address two or more conflicting objectives simultaneously and produce a set of Pareto-optimal solutions. MOO algorithms use an objective function vector that is minimized or maximized based on decision variables.

Multi-objective problems often involve both inequality and equality constraints [9,12]. The collection of all Pareto-optimal solutions is referred to as the Pareto front or frontier[13,14]. MOO techniques are generally categorized as either evolutionary methods[10] or swarm-based methods[14, 15]. Notable evolutionary-based techniques include the Non-Dominated Sorting Genetic Algorithm II (NSGA-II) and the Non-Dominated Sorting Genetic Algorithm III (NSGA-III). Swarm-based techniques [11,15] are recognized for their simplicity and robustness in identifying optimal solutions. Multi-objective Particle Swarm Optimization (MOPSO) [14] is a prominent example of a swarm-based multi-objective optimization technique. Algorithms that employ Pareto optimal solution strategies, such as NSGA-II, NSGA-III[15], the Pareto Strength Evolutionary Algorithm (SPEA), MOPSO, and Multi-Objective Evolutionary Algorithms (MOEAs)[14], are widely utilized in microgrid applications.

MOO algorithms are capable of managing large-scale Microgrids (MGs) and addressing constraints such as power limitations in MGs and load power shortages. In comparative analyses of MOO algorithms for MG applications, the most prominent techniques are MOPSO, NSGA-II, artificial bee colony (ABC), and SPEA2 [16–21]. Various unique MOO approaches are applied, utilizing real-time data to address load and demand balancing within the system. Additionally, a real-time power hardware-in-the-loop (PHIL) system is discussed, in which an adaptive weighted method is employed to optimize the size of DERs and to control variables such as the state of charge (SOC) of the battery [22].

In this research, our objective was to optimize a physically constrained microgrid with complex operating conditions, including SOC, curtailment, and demand mismatch. We tried to fill the gap with an energy model and complex engineering constraints. Although several MOO algorithms have been widely applied [7,21,23–27], MOEA/D was selected due to its decomposition-based structure, which enables controlled trade-off exploration and stable convergence under constrained EMS conditions. Its neighborhood-based updates and compatibility with surrogate-assisted evaluation make it suitable

 doi:10.20944/preprints202603.2378.v1

for integrating physical replay validation and decision-oriented optimization in MG applications [28]. Also the wide use of evolutionary optimization in EMS research, there remains a gap of experimentally validated, unified frameworks that connect microgrid and smart-grid (SG) operation using real hardware and data-driven evaluation. For this reason we setup an experimental integration and validation of evolutionary multi-objective optimization within practical EMS environments. The SG test bench was (figure 3) used as a hardware platform that enables integration and switching of multiple energy sources, allowing controlled evaluation of microgrid EMS behavior under realistic operating conditions.

The structure of this paper is as follows. Section I presents an overview of MGs, emphasizing their challenges and the importance of multi-objective optimization techniques in recent years. Section II details the experimental setup, and Section III outlines the problem formulation and proposed methodology. Section IV baseline Optimization frameworks, Section V reports the results and critical discussion, while Section VI provides a conclusion, respectively. Furthermore, the paper is organized according to the following key objectives:

(a) The objective was to develop an experimental setup (figure 3) capable of efficiently logging and recording operational data, while ensuring reliable integration between the OPAL-RT-PHIL and the SG test bench. The SG configuration comprised a photovoltaic system, a battery, an inverter, and a load system.

(b) This study analyzes and compares the system's performance in both grid-connected and islanded conditions. It also evaluates how the MOEA/D optimization algorithm affects the overall performance and stability of the MG.

(c) This study looks at how a surrogate-assisted, knee-guided multi-objective optimization framework finds the best operating regions under different system conditions using real measurement data. Instead of controlling systems in real time, the framework helps with energy management decisions by quickly exploring possible solutions and selecting compromise solutions under system constraints in both grid-forming and grid-connected microgrids [29].

(d) This research addresses the limitations present in current MOO methods for MG applications and examines how surrogate techniques can accelerate convergence. Preference-based and knee-based methods were also evaluated to maintain robustness.

(e) The proposed strategy was validated using evaluation metrics and compared with two baseline methods selected for this study. We used MOEA/D for all methods to keep the comparison fair. This way, any improvement comes from our proposed ideas (smart seeding, surrogate, knee guidance), not from changing the algorithm itself.

(f) This study uses OPAL-RT microgrid power hardware-in-the-loop (PHIL) experiments and a Lucas-Nülle smart-grid lab [30] platform (table 1) to explore EMS optimization in different operating modes. Three experiments are carried out. Section A tests a physically based EMS approach with OPAL data. Section B uses smart-meter data and Gaussian Process models for surrogate-assisted optimization. Section C adds economic cost, degradation, and reliability goals, using Random Forest surrogate modeling and statistical evolutionary multi-objective evaluation metrics.

 doi:10.20944/preprints202603.2378.v1

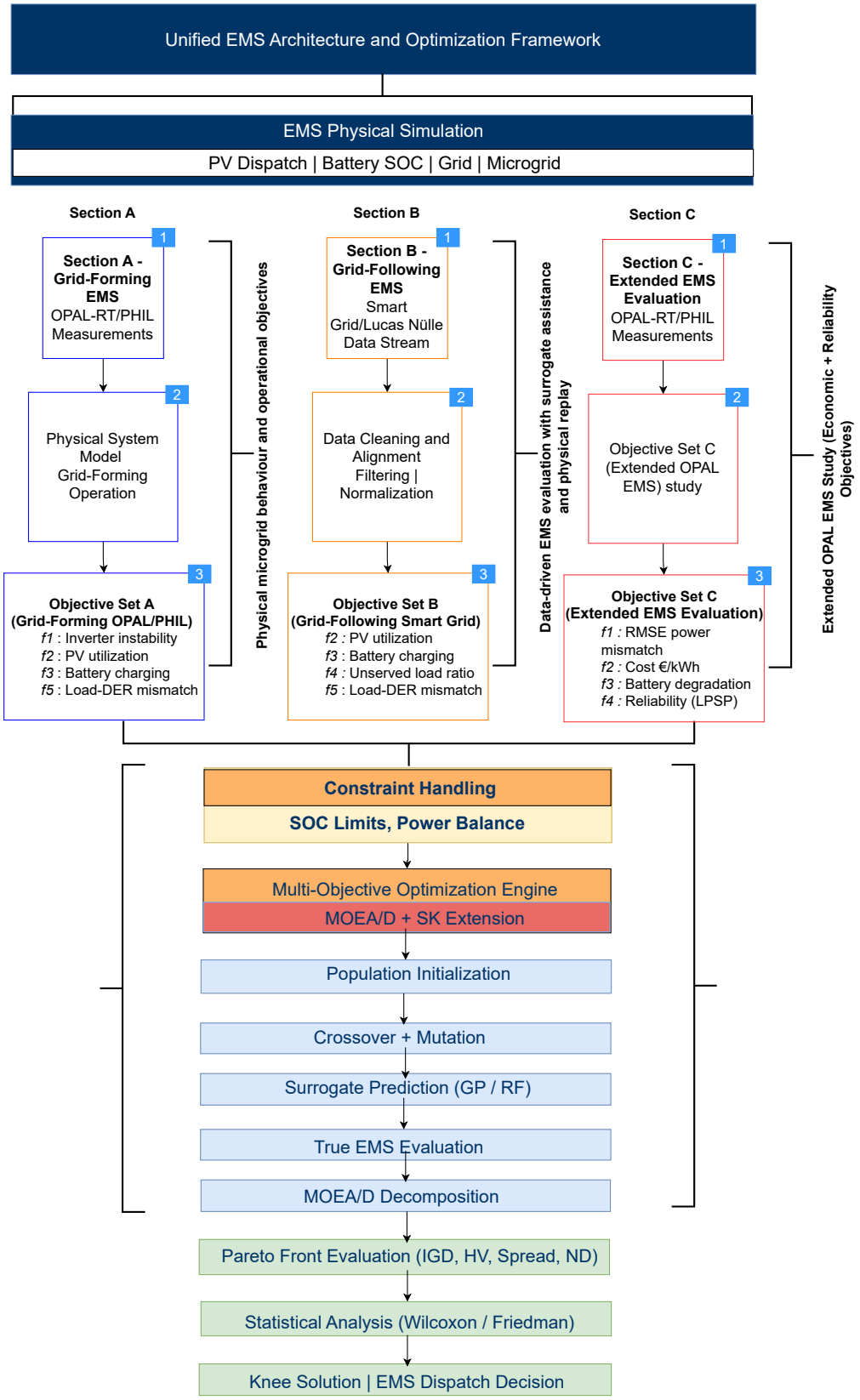

Figure 1. Surrogate-Assisted Knee-Guided MOEA/D Energy Management Framework

 doi:10.20944/preprints202603.2378.v1

Table 1. System constraints, decision bounds, and operational parameters

Parameter	Value	Description
Decision variable bounds		
PV_{sup}	$[0, 1500]$ W	PV dispatch limit.
$BATT_{\text{sup}}$	$[0, 500]$ W (A,B)	Battery support (technical studies).
	$[-500, 500]$ W (C)	Charging/discharging (extended study).
$OPAL_{\text{sup}}$	$[0, 500]$ W	Grid/OPAL support limit.
$CURT$	$[0, 1500]$ W	Curtailment ($\leq PV$ enforced).
SOC	$[40, 100]$% (A,C)	PHIL battery constraints.
	$[10, 100]$% (B)	Smart-grid dataset constraint.
d_{pv}	$\{0, 1\}$	PV activation switch.
Hardware / physical settings		
Load reference	1200 W	Nominal load.
Inverter efficiency	0.95	Conversion efficiency.
Voltage	230 V	Nominal AC voltage.
Current	3.0 A	Nominal AC current.
Battery capacity	2443 Wh	Used for SOC and degradation.
η_{ch}, η_{dis}	0.95	Charge/discharge efficiencies.
Sampling time	1 s	Data logging interval.
Section C economic parameters		
Energy cost	0.22–0.30 €/kWh	Grid/OPAL energy cost.
Battery degradation	0.08 €/kWh	Throughput-based cost.
Unserved penalty	2.00 €/kWh	Reliability penalty.
Curtailment penalty	0.03 €/kWh	Renewable curtailment penalty.

2. Experimental Setup and Data Acquisition

To establish the Data Acquisition Framework for Microgrid Optimization an experimental setup has been established (figure 3). The table 2 show the specific attributes used in the experiments. The attribute criteria remained the same during grid-connected mode. The only change was that Microgrid Output (Field 2) was replaced with grid output data (Field 4).

Table 2. Microgrid Data Column Mapping Based on Measurement Source

Component	Raw Column Name	Description
Inverter + PV (Field 1)		
	1_INV_PV_P_SUM	Inverter output power (W)
	1_INV_PV_PV_P_SUM	PV panel power (W)
	1_INV_PV_V_L1	Inverter voltage (V)
	1_INV_PV_I_L1	Inverter current (A)
	1_INV_PV_FREQ	Inverter frequency (Hz)
	1_INV_PV_PF_L1, L2, L3	Power factor per phase
	1_INV_PV_P_L1, L2, L3	Active power per phase (W)
Load (Field 5)		
	2_Load_P_SUM	Total load power (W)
	2_Load_V_L1	Load voltage (V)
	2_Load_I_L1	Load current (A)
	2_Load_PF_L1	Load power factor
Microgrid Output (Field 2)		
	3_Microgrid_P_SUM	Microgrid output power (W)
	3_Microgrid_V_L1	Microgrid voltage (V)
	3_Microgrid_FREQ	Microgrid frequency (Hz)
	3_Microgrid_I_L1	Output current to grid (A)
	3_Microgrid_PF_L1	Output power factor

 doi:10.20944/preprints202603.2378.v1

Table 2. *Cont.*

Component	Raw Column Name	Description
Battery System (Field 3)		
	4_Battery_P_SUM	Battery power (W)
	4_Battery_V_L1	Battery voltage (V)
	4_Battery_I_AVG	Battery average current (A)
	4_Battery_PF_SUM	Battery power factor
	4_Battery_P_L1, L2, L3	Active power per phase (W)
	4_Battery_VARQ1_SUM	Reactive power (VAR)
	4_Battery_V_LN_AVG	Line-neutral voltage (avg) (V)
PV System from OPAL-RT		
	OPAL_PV_Current	PV current (A)
	OPAL_PV_Voltage	PV voltage (V)
Battery SOC (OPAL-RT)		
	OPAL_Battery_SOC	State of charge (SOC, 0–100%)

2.1. OPAL-RT Microgrid Platform (Grid-Forming)

In this configuration, the MG functions as a Power Hardware-in-the-Loop (PHIL) test bench. The table 2 categorizes raw columns from both Lucas-Nülle smart grid meters and OPAL-RT real-time simulator into their respective microgrid components.

2.2. Lucas–Nülle Smart-Grid Platform (Grid-Following)

The SG system was configured (figure 3) to enable simultaneous connection and operation of all resources. The setup includes DERs such as PV systems, a grid-tied inverter, the utility grid, loads, and a microgrid. In the experimental setup, multiple SG components and an OPAL-RT real-time simulator [31] are integrated to provide real-time dataset for Energy Management (EM) optimization [32,33]. The three-phase power distributed within the SG panel is managed by two bus-bar configurations. Isolators enable switching between bus bars to control both incoming and outgoing power feeders and to facilitate bus-bar changes. The switching mechanism is implemented using three switches, designated as q1, q2, and q3. The bus-bar system is divided into input 1 and input 2, each providing L1, L2, and L3 lines. Activation of control panel q1 energizes bus-bar line 1 and isolates it from q2. Additionally, control panel q3 functions as a circuit breaker, serving as the outgoing field for connecting outgoing feeders. In coupling scenarios, q3 connects the isolators to couple the bus bars (figure 3). The energy storage system (ESS) utilizes a lithium-ion battery with a nominal capacity of 2443 Wh. The multidirectional converter operates at a rated voltage of 230 V and a rated power of 9 kVA. The battery charging and discharging processes are controllable and can be managed either manually or automatically. The system's DC input voltage range is 250 V to 1000 V, while the maximum power point (MPP) voltage range is 300 V to 800 V. The maximum DC current is 11 A. The inverter provides a maximum AC output of 3200 W with a maximum current of 7 A. The resistive load was variable and supplied 3-phase 1 kW to the system, while the capacitive (1 kW) and inductive (1 kW) loads were fixed and not controllable. To apply the optimization technique in a realistic scenario, transmission line models of 150 km and 300 km were used, with resistances per phase of 3.6 ohms and 7.2 ohms. In this research, the PV system serves as the primary power supply component for the DERs, with a solar altitude emulator used to replicate solar conditions. A three-phase industrial PV inverter is employed, and the solar panel emulator is capable of simulating up to 1.5 kW of power.

2.3. Measurement Data and Prepossessing

This study employed a data collection approaches to obtain real-time data such as state of charge (SOC), battery voltage, and current from Lucas Nülle (LN) SG components. For real-time monitoring and optimization, a communication channel (figure 3) was established using Modbus TCP.

 doi:10.20944/preprints202603.2378.v1

The supervisory control and data acquisition (SCADA) system was implemented to collect data from DERs, including PV systems, ESS, inverters, and the utility grid (figure 2).

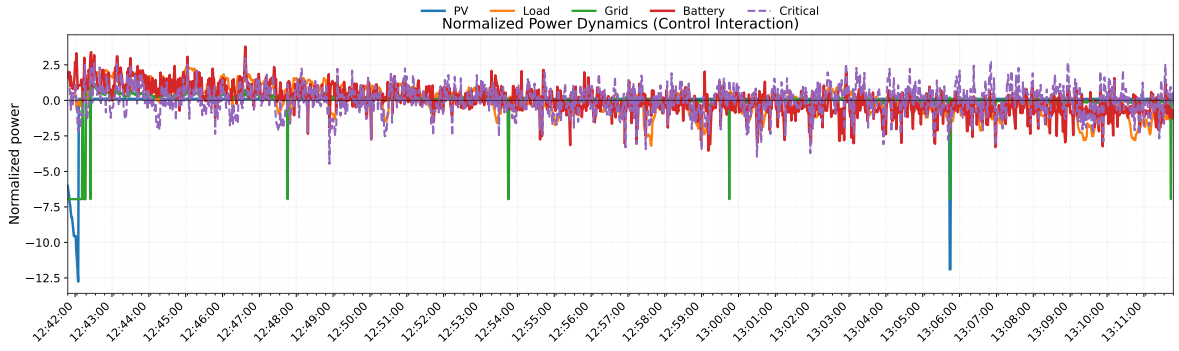

Figure 2. Multi-axis data visualization results obtained during the data collection process from the experimental system over time

The figure 2 shows the data visualization before applying the MOO techniques. The figure shows how key power components in the hybrid energy system change over time (presented with a resolution of 1 minute). These include PV generation, load demand, grid exchange, battery dispatch, and critical load. The results show that grid power and battery dispatch are closely linked over time. In that plot we can see the PV generation changes a lot, while critical load stays mostly steady in the EM plan. The time axis captures short-term changes and quick control response at how the system operates.

3. EMS Problem Formulation

Multi-objective optimization plays a crucial role in solving real-world engineering problems [34,35], where objectives are often conflicting such as, optimizing between energy efficiency and cost, or between reliability and sustainability in microgrid systems. To address complex technical constraints in optimization, this research uses a hybrid approach. In this work, a Surrogate-Assisted, Knee-Preserving Evolutionary Algorithm (SK-MOEA) with Stochastic-Elitist Survival is used for MOO. While classical MOO algorithms, such as NSGA-II and NSGA-III, provide robust Pareto front approximations, they often fail to incorporate human-relevant decision metrics, including trade-offs or knee points. Moreover, purely elitist survival strategies can degrade performance in many-objective and multi-modal spaces [36].

The proposed SK-MOEA/D framework represents a hybrid extension of MOEA/D, integrating surrogate-assisted evaluation and knee-point-based decision prioritization. The framework was designed for EMS decision support rather than introducing a fundamentally new evolutionary algorithm. It is addressed complex microgrid energy management systems that use hardware-in-the-loop setups. This idea incorporates traditional MOEAs by focusing on decision-relevant solutions, maintaining solution diversity, and speeding up convergence with learned surrogates. This work builds on the EMS framework and flow chart (1), following Section A (MG Grid-forming EMS) and Section B (Grid-following SG EMS). In Section C, a extended objective formulation is introduced for economic and reliability analysis, while keeping the main structure the same.

Our method addresses five complex and conflicting objectives, as well as nonlinear and operational EMS constraints. In the process of EMS, the objective parameters were included in reference directions and the trade-offs. To capture the all controllable variables such as PV power battery charge/discharge, inverter operation and MG production as decision vector has been formulated. In the objective vector the complex constraints such as SOC dynamics, power balance has been adapted.

 doi:10.20944/preprints202603.2378.v1

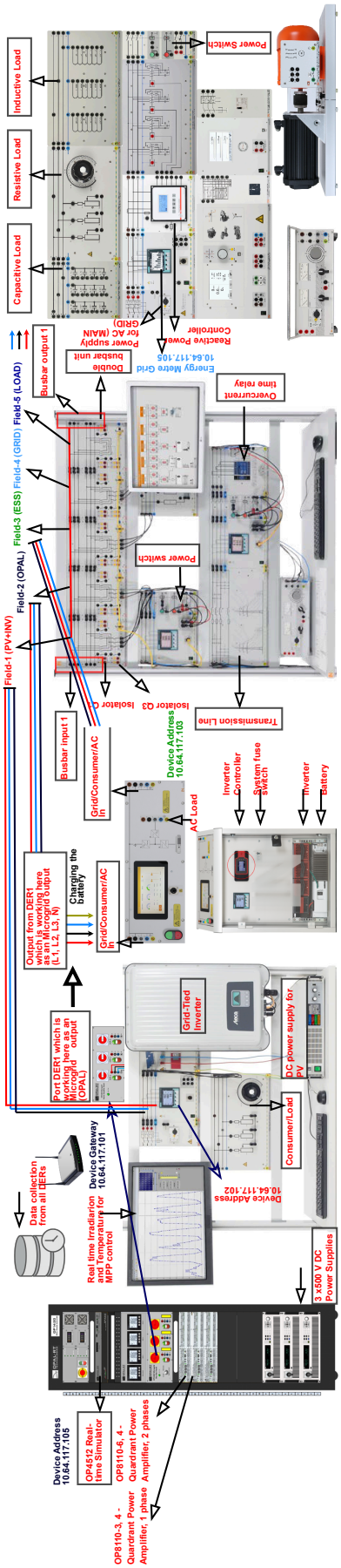

Figure 3. Experimental setup for data acquisition including distributed energy resources (DERs)

 doi:10.20944/preprints202603.2378.v1

Decision Variables

To formulate the MOO problem the decision vector which has been taken as follows :

$$\mathbf{x} = [P_{PV}, P_{bat}, P_{inv}, P_{opal}, SOC, \delta_{inv}, \delta_{PV}]^T \tag{1}$$

Where P_{PV} is the PV output power (W) representing the total power generated during the grid (when the utility grid is on) or without a grid (when OPAL MG is on) connection system by using the PHIL test bench. The PV generation also depends on the real-time solar radiation, which is also controllable. The P_{bat} represents the battery charging/discharging power (W) during battery activation with the smart grid system. P_{inv} is the Inverter output power (W), which is connected to convert DC to AC output power as an input in the smart grid bus-bar system. To generate the output power from the MG, a P_{opal} OPAL-based support power for charging (W) has also been connected into the SG system. The SOC represents the State of charge (SOC) of the battery (%) where δ_{inv} is the binary status of the inverter (1 = ON, 0 = OFF) and δ_{PV} is the binary status of PV availability (1 = ON, 0 = OFF). In addition, the capacity shortage is given by $P_{\text{sup}} = PV_{\text{sup}} + BATT_{\text{sup}} + OPAL_{\text{sup}}$. When $f_4 = 0$, the load is fully covered. Higher values indicate a supply deficit.

Technical Objectives Functions for Section A and B

In this part, the objective functions for grid-forming and grid-following and also the extended objective to validate the reliability and economic feasibility, have been formulated.

Objective 1: Minimize inverter instability

$$f_1(\mathbf{x}) = |P_{inv} - V_{inv} \cdot I_{inv} \cdot \eta_{inv}|^2 \tag{2}$$

Objective 2: Maximize PV utilization

$$f_2(\mathbf{x}) = -P_{PV} \cdot \delta_{PV} \tag{3}$$

Objective 3: Maximize battery charging (from OPAL)

$$f_3(\mathbf{x}) = -\left(P_{bat}^{+} + P_{opal}\right) \cdot \delta_{inv} \tag{4}$$

Objective 4: Minimize Unserved Load Ratio

$$f_4(\mathbf{x}) = 1 - \frac{P_{\text{sup}}(\mathbf{x})}{P_{\text{load}}} \tag{5}$$

Objective 5: Minimize load–DER mismatch

$$f_5(\mathbf{x}) = \left|P_{load} - (P_{PV} + P_{bat} + P_{opal})\right|^2 \tag{6}$$

Operational Constraints and Power-Balance Model

$$P_{load} = P_{PV} + P_{bat} + P_{opal} + \epsilon \quad (\epsilon \text{ within acceptable tolerance}) \tag{7}$$

$$SOC_{t+1} = SOC_t + \frac{\eta_{ch} \cdot P_{bat}[t] \cdot \Delta t}{C_{bat}} \quad \text{if } P_{bat}[t] > 0 \tag{8}$$

this equation represents the $[SOC_t]$ State of charge at the current time step t, expressed as a percentage. Where $[\eta_{ch}]$ presents the Charging efficiency of the battery system (typically $0.9 \leq \eta_{ch} \leq 1.0$). In addition, $[P_{bat}[t]]$ presents the battery charging power at time t, which measured in watts. Positive values indicate charging. Also $[\Delta t]$ is the time interval between successive measurements or updates, in hours and $[C_{bat}]$ is the total capacity of the battery in watt-hours (Wh). This equation

 doi:10.20944/preprints202603.2378.v1

quantifies how the SOC increases based on the energy input over a time step, adjusted for charging efficiency and battery capacity.

$$40\% \leq SOC_t \leq 100\% \tag{9}$$

$$0 \leq P_{PV}, P_{opal}, P_{inv} \leq P_{rated} \tag{10}$$

$$\delta_{inv}, \delta_{PV} \in \{0,1\} \tag{11}$$

The inverter activation variable δ_{inv} is modeled as a binary control signal measured by real-time operational conditions. The PV–inverter coupling is expressed as

$$\delta_{inv} = 1 \;\Rightarrow\; P_{PV}^{used} > 0 \tag{12}$$

and the inverter status is defined by

$$\delta_{inv} = \begin{cases} 1, & \text{if } V_{inv} > V_{min} \text{ and } SOC > SOC_{min} \\ 0, & \text{otherwise} \end{cases} \tag{13}$$

Section C Extended EMS Objectives

$$x^{(C)\star} = \arg\min_{x \in \Omega^{(C)}} \mathbb{E}_k \Big[g_k\Big(F^{(C)}(x) + \lambda_{CV} CV(x)\mathbf{1} \Big) - \beta \kappa_n(x) - \delta D_n(x) + \alpha U_n(x) \Big] \tag{14}$$

where the objective vector is defined as

$$labeleq : unified2F^{(C)}(x) = \begin{bmatrix} \frac{1}{1000}\sqrt{\frac{1}{T}\sum_{t=1}^{T}\left(P_{load}(t) - P_{sup}(t)\right)^2} \\ \frac{c_{buy}E_{imp} - c_{sell}E_{exp} + 12c_{demand}P_{peak,imp}}{E_{load} + \epsilon} \\ \frac{\sum_{t=1}^{T} \frac{|P_{bat}(t)|\Delta t_{hr}}{1000}}{2E_{bat} + \epsilon} \\ \frac{E_{unserved}}{E_{load} + \epsilon} \end{bmatrix} \tag{15}$$

subject to the EMS physical model

$$P_{sup}(t) = a_{pv}(t)P_{PV}^{avail}(t) - a_{curt}(t)a_{pv}(t)P_{PV}^{avail}(t) + a_{bat}(t)P_{bat}^{max} + a_{opal}(t)P_{opal}^{max} \tag{16}$$

$$e(t) = P_{load}(t) - P_{sup}(t) \tag{17}$$

$$SOC(t+1) = SOC(t) - \frac{\max(P_{bat}(t),0)\Delta t_{hr}}{E_{bat}\eta_{dis}} + \frac{\max(-P_{bat}(t),0)\eta_{ch}\Delta t_{hr}}{E_{bat}} \tag{18}$$

$$SOC_{min} \leq SOC(t) \leq SOC_{max} \tag{19}$$

The objective functions in Section C were restructured into normalized forms to ensure comparability across technical, economic, and reliability criteria. The power mismatch objective was defined as the root mean square (RMS) of the load–supply imbalance, $f_1'(x) = \frac{1}{1000}\sqrt{\frac{1}{T}\sum_{t=1}^{T}\left(P_{load}(t) - P_{sup}(t)\right)^2}$, which minimizes the deviation between demand and supplied power. The economic objective was expressed as $f_2'(x) = \frac{C_{op,yr}}{E_{load}+\epsilon}$, where the annual operating cost is given by $C_{op,yr} = (c_{buy}E_{imp} - c_{sell}E_{exp}) + 12c_{demand}P_{peak}$, with c_{buy}, c_{sell}, and c_{demand} representing import tariff, export tariff, and demand charge, respectively. The cost term may become negative when export revenue exceeds import cost, representing a profit scenario rather than a modeling inconsistency. The battery degradation objective also

 doi:10.20944/preprints202603.2378.v1

modeled as $f_3'(x) = \frac{E_{throughput,yr}}{2E_{bat}+\epsilon}$, approximating the equivalent full cycle (EFC) count based on total battery energy throughput (table 7). The reliability objective has been defined as $f_4'(x) = \frac{E_{unserved}}{E_{load}+\epsilon}$, corresponding to the loss-of-power-supply probability (LPSP), which quantifies the ratio of unmet demand to total load. Here, E_{imp} and E_{exp} denote imported and exported energy, E_{load} is the total load demand, $E_{unserved}$ is the unmet energy, and P_{peak} represents the peak demand. Positive P_{bat} denotes battery discharge, while negative values indicate charging.

The (equation 14) $x^{(C)}$ denotes the Section C block-based dispatch vector, $P_{PV}^{avail}(t)$ is the available PV power, $P_{load}(t)$ is the measured load demand, $P_{bat}^{\max}$ and $P_{opal}^{\max}$ are the battery and OPAL rated powers, Δt_{hr} is the sampling interval in hours, E_{bat} is the battery energy capacity, η_{ch} and η_{dis} are the battery charge and discharge efficiencies, and λ_{CV} is the penalty coefficient used to embed constraint violations into the objective vector. The λ_{CV} is the constraint penalty coefficient. In this study $\lambda_{CV} = 10^3$ is used to penalize infeasible solutions that violate SOC limits or power balance constraints. Constraint violations are aggregated using

$$CV(x) = CV_{bal}(x) + 10^3 CV_{soc}(x) \tag{20}$$

and incorporated into the objective vector as

$$F_{pen}(x) = F^{(C)}(x) + \lambda_{CV} CV(x)\mathbf{1} \tag{21}$$

Table 3. Unified optimization and framework configuration for MOEA/D-based EMS (Sections A–C)

Parameter	Value	Description
General settings		
Generations	$G_{\max} = 120$	Fixed termination criterion in all sections.
Objectives	$M = 4$	Four-objective formulation (section-dependent).
Independent runs	$R = 20$	Statistical evaluation using 20 seeds.
Seed policy	$\{0, \ldots, 19\}$	Same seeds for all methods and sections.
Section-dependent problem settings		
Population size	A/B: $N = 120$; C: $N = \lvert\text{ref\_dirs}\rvert$	A/B use population size 120; Section C population is determined by Das–Dennis reference directions.
Decision variables	$n = 6$	6-variable EMS vector
Reference directions	A/B: $(H = 7)$; C: $(H = 12)$	Section C uses a denser decomposition setting.
MOEA/D configuration		
Decomposition	PBI	Penalty-based boundary intersection.
Neighborhood size	$T = 15$ / 20	Baseline: 15, SK-MOEA/D: 20.
Mating probability	0.7 / 0.9	Baseline vs SK-MOEA/D.
Sampling	Random bounded/data-informed fixed sampling	Baseline: random bounded initialization; Smart-Seed uses structured fixed sampling from feasible patterns.
Constraint handling	Repair + penalty	Physical feasibility enforced in decision space.
Framework activation		
Section A	$\{f_1, f_2, f_3, f_5\}$	Physical evaluation only (no surrogate).
Section B	$\{f_2, f_3, f_4, f_5\}$	GP surrogate + physical replay + TOPSIS.
Section C	$\{f_1', f_2', f_3', f_4'\}$	Extended objectives + RF + stochastic survival.
Physical replay	B active; C not used as final replay	Section B includes explicit replay validation; Section C enforces feasibility through the optimization model and penalties.

 doi:10.20944/preprints202603.2378.v1

MOEA/D-Based EMS Optimization Framework

This research illustrates real-time MOO techniques for EMS control by actively prioritizing decision variables. While previous studies have focused on theoretical aspects [36–40] this work implements real-time energy management constraints within an evolutionary framework. Although classical MOEA/D demonstrates robust decomposition-based convergence, but it can allow to premature convergence under strict constraints. Furthermore, conventional termination criteria can lead to inefficiency in real-time MG environments. To resolve these challenges, we develop an integrated EMS-aware evolutionary framework. Whether the knee-point preservation mechanism is used to retain the decision-relevant solutions and surrogate modeling is used to guide candidate evaluation in PHIL systems [12].

The proposed EMS optimization framework evolves across three stages. Section A employs surrogate-free MOEA/D-based optimization for the technical OPAL study. Section B introduces Gaussian-Process -assisted optimization with physical replay in the grid-following scenario. Section C implements the Random-Forest-assisted SK-MOEA/D framework, including knee-guided stochastic survival and statistical EMO evaluation. The framework is built and tested step by step to make sure each part is clearly and fairly tested. By following this staged approach, we can see how each part contributes, and then everything functions together (table 3).

Experimental Design and Evaluation Protocol

Section A: OPAL Physical EMS Study

In the first part of this work, we used a grid-forming EMS with OPAL-RT hardware-in-the-loop measurements. A multi-objective MOEA/D optimizer was applied to evaluate objectives like inverter stability, renewable use, and load balance. The Algorithm 1 represents the workflow of the Grid-Forming optimization process.

Algorithm 1 Knee-Guided MOEA/D Framework for Section A (Grid-Forming Technical Objectives)

Require: Population size N, reference directions Λ, neighborhood size T, maximum generations $G_{\max}$
Ensure: Pareto front approximation for $\{f_1, f_2, f_3, f_5\}$
Initialize population $P = \{x_1, x_2, \ldots, x_N\}$ within decision bounds
Repair each candidate to satisfy physical bounds and $CURT \leq PV$
Evaluate true objectives $F(x_i) = [f_1, f_2, f_3, f_5]$ for all $x_i \in P$
for $g = 1$ to $G_{\max}$ **do**
    for each subproblem i associated with reference direction λ_i **do**
        Select parents from the neighborhood of subproblem i
        Generate offspring y using SBX and mutation
        Repair y to satisfy physical feasibility and variable bounds
        Evaluate true objectives $F(y)$ using the Section A physical EMS model
        Update neighboring subproblems using MOEA/D decomposition (PBI)
    end for
    Extract the current non-dominated set $P^{ND} \subseteq P$
    Normalize objective values of P^{ND}
    Identify knee candidates from P^{ND} using distance-to-ideal / trade-off prioritization
end for
Select the final representative knee solution from the non-dominated set
return final non-dominated set P^* and knee solution x^{knee}

Section B: Smart-Grid Surrogate and Replay Study

In the second part, we introduced a grid-following EMS framework based on real smart-meter data. Gaussian-process (GP) surrogate models were used to approximate physical objectives, which allowed for surrogate-assisted MOEA/D optimization.

We then filtered surrogate solutions via physical replay under realistic conditions, and knee-guided selection enabled a feasible EMS dispatch decision under physical constraints (figure 1). The Algorithm 2 represents the workflow of the Grid-Following optimization process.

 doi:10.20944/preprints202603.2378.v1

Algorithm 2 Surrogate-Assisted MOEA/D Framework for Grid-Connected EMS (Section B)

Require: Population size N, reference directions Λ, generations G
Ensure: Pareto front approximation for $\{f_2, f_3, f_4, f_5\}$
Initialize population $P = \{\mathbf{x}_1, \ldots, \mathbf{x}_N\}$ within decision bounds
Evaluate physical objectives $F(\mathbf{x}_i)$ for all $\mathbf{x}_i \in P$
Train initial surrogate models $\hat{f}_k(\mathbf{x})$, $k \in \{2, 3, 4, 5\}$
for $g = 1$ to G **do**
    Predict objective values $\hat{F}(\mathbf{x})$ using surrogate models
    Select candidate subset for exact physical evaluation
    Evaluate selected candidates using the physical EMS model
    Update surrogate models with new data
    Identify knee solutions on the current Pareto front
    Compute diversity indicators on the current population
    Generate offspring using MOEA/D variation operators
    Update neighboring subproblems using MOEA/D decomposition
end for
Perform physical replay on selected Pareto candidates
Extract final non-dominated set P^*
Select the final EMS operating point using TOPSIS
return P^*

Section C: Extended EMS Statistical Study

In the third part, the hardware setup remained unchanged, but we changed the objectives compared to section A (Grid-forming) and B (Grid-following), which focused more on the reliability of the MG system (figure 1). The workflow for Section C is shown in Algorithm 5.

The process begins with OPAL data prepossessing and EMS simulation, then evaluates the updated objective set $F^{(C)}(x)$, applies constraint penalties, and finally uses surrogate-assisted multi-objective optimization with Random Forest-based SK-MOEA/D. Sections A and B focus on operational goals like inverter stability and DER coordination. In contrast, the extended evaluation in Section C looks at system-level indicators such as power mismatch, economic cost, battery degradation, and reliability. This broader approach allows the SK-MOEA/D framework to be tested under a more comprehensive multi-objective EMS setup.

4. Baseline Optimization Frameworks

This study utilizes two baseline multi-objective evolutionary algorithms. Identical parameters (table 1, 3) were maintained in both cases to prevent misleading indications of algorithm 3, algorithm 4. These algorithms include MOEA/D and its data-informed variant, Smart-Seed MOEA/D. Both are designed to optimize the steady-state operation of the hybrid microgrid by simultaneously minimizing multiple conflicting objectives that are derived from measured system variables. MOEA/D was employed as a consistent optimization framework across all experimental variants to maintain controlled and equitable comparisons.

The baseline MOEA/D, Smart-Seed MOEA/D, and SK-MOEA/D differ exclusively in their initialization strategies, surrogate assistance, and knee-guided selection mechanisms. This experimental design ensures that observed differences in HV, mismatch, and solution characteristics can be attributed to the proposed methodological innovations rather than to differences in algorithmic structure.

Baseline MOEA/D

The Multi-Objective Evolutionary Algorithm based on Decomposition (MOEA/D) decomposes the vector problem into N scalar sub-problems. Each sub-problem is defined by a weight vector λ^i and optimized through the Penalty-based Boundary Intersection (PBI) function [41]:

$$g^{te}(x \mid \lambda^i, z^*) = d_1 + \theta d_2, \tag{22}$$

 doi:10.20944/preprints202603.2378.v1

where

$$d_1 = \frac{|(F(x) - z^*)^T \lambda^i|}{\|\lambda^i\|}, \tag{23}$$

$$d_2 = \left\| F(x) - \left(z^* + d_1 \frac{\lambda^i}{\|\lambda^i\|} \right) \right\|. \tag{24}$$

Here z^* is the current ideal point (the component-wise minimum of all evaluated solutions) and θ is the aggregation penalty parameter that balances convergence and diversity. Each sub-problem maintains a neighborhood $B(i)$ of weight vectors. For every generation g, differential evolution crossover and polynomial mutation [42] are applied within $B(i)$ to produce offspring y. If the neighbor x^k is replaced by y [43,44].

$$g^{te}(y \mid \lambda^i, z^*) < g^{te}(x^k \mid \lambda^i, z^*), \quad \forall k \in B(i),$$

Constraint violations are penalized directly in the scalarized objective:

$$g^{con}(x) = g^{te}(x) + \sum_{j=1}^{n_g} \mu_j \max(0, g_j(x))^2 + \sum_{k=1}^{n_h} \nu_k |h_k(x)|,$$

where $g_j(x)$ and $h_k(x)$ represent inequality and equality constraints such as SOC bounds and inverter limits. This ensures that infeasible candidates are dominated while still allowing exploration near constraint boundaries [43,44].

Algorithm 3 MOEA/D for Technical Multi-Objective Optimization

Require: Population size N, maximum generations G, reference directions Λ, neighborhood size T
Ensure: Pareto front approximation for $\{f_1, f_2, f_3, f_5\}$
Initialize population $P = \{x_1, x_2, \ldots, x_N\}$ within variable bounds
Evaluate objectives $F(x_i) = [f_1, f_2, f_3, f_5]$ for all $x_i \in P$
Define neighborhood $B(i)$ for each subproblem i based on Λ
for $g = 1$ to G **do**
    for each subproblem i **do**
        Select parent solutions from $B(i)$
        Generate offspring y via crossover and mutation
        Evaluate $F(y) = [f_1, f_2, f_3, f_5]$
        if y violates constraints **then**
            Repair or discard y according to feasibility rules
        end if
        Update neighborhood $B(i)$ if y improves decomposition metric
    end for
end for
return Final non-dominated set P^*

Smart-Seed MOEA/D

The Smart-Seed MOEA/D method serves as a baseline because it uses real data to seed the population, not random values [35,45]. The first individuals were created using actual microgrid operating data from the OPAL-RT hardware platform and the Smart Grid meter system [45,46]. Instead of using only random sampling within bounds B, the initial population is created with a seeding strategy based on historical or measured system data $\mathcal{D}$. If we consider the relevant operational variables as

$$\mathcal{C} = \{P_{\text{PV}}, P_{\text{BATT}}, P_{\text{OPAL}}, \text{SOC}\}.$$

From $\mathcal{D}$, feasible and stable records are extracted, normalized to $[0, 1]$, and used to build a sampling matrix X_0:

$$X_0 = \texttt{SmartSeedSampling}(B, \mathcal{D}, \mathcal{C}),$$

 doi:10.20944/preprints202603.2378.v1

where the sampling density is biased toward regions with high renewable utilization and low mismatch. This population replaces the random initialization of the baseline MOEA/D. After initialization, Smart-Seed MOEA/D follows the same evolution, evaluation, and replacement procedures as the baseline algorithm: the PBI decomposition in Eq. (22), constraint handling via penalization, and neighborhood replacement rules remain unchanged. The modified seeding maintains and convergence speed without altering the mathematical structure of the algorithm [41,47].

Algorithm 4 Smart-Seed MOEA/D with Rule-Based Initialization

Require: Population size N, reference directions Λ, smart-seed ratio α, heuristic rules R
Ensure: Improved convergence and diversity for $\{f_1, f_2, f_3, f_5\}$
Determine number of rule-based seeds $N_r = \alpha N$
Generate N_r smart seeds using rules R and historical data:
    Enforce SOC and power-balance feasibility
Generate $(N - N_r)$ random individuals within system bounds
Combine all solutions into initial population $P = P_{\text{smart}} \cup P_{\text{rand}}$
Evaluate real objectives $F(x_i) = [f_1, f_2, f_3, f_5]$ for all $x_i \in P$
Define neighborhoods $B(i)$ for each subproblem based on Λ
for generation $g = 1$ to G **do**
    for each subproblem i **do**
        Select parent solutions from $B(i)$
        Generate offspring via crossover and mutation
        Evaluate $F(y)$ and apply feasibility repair if necessary
        Update neighbors if y improves decomposition metric
    end for
    Optionally update rules R or resample smart seeds based on new data
end for
return Final non-dominated set P^*

SK-MOEA/D Optimization Framework

In the figure 4, it illustrates the operation integrated in the methodology in the MG optimization context. The solutions (blue) represent actual objective evaluations based on system parameters such as photovoltaic generation, battery power, and load balance. Surrogate estimates (oranges) approximate these solutions, reducing computational burden [47]. The knee point (red) indicates a trade-off solution where PV utilization is high, while the load-DER mismatch remains acceptably low. Survival candidates (green) highlight the stochastic elitist mechanism that balances exploration of promising solutions with exploration of diverse ones. To explain the methods this schematic has been presented which reflects the interaction of objectives derived from real MG system in this research.

In this method the reference directions [28] and partitions has been followed a discretion in the objective space. The association of the each individuals in the population point are linked to its nearest reference direction to select survivors per direction. The reference directions corresponds to a preference vector in the objective space. Based on this research it corresponds to the maximizing the PV utilization and battery charging while minimizing mismatch. On the other hand the Knee-point direction [37,48] in the Pareto front determines the operating conditions of the MG, where objectives such as PV utilization, load balancing, and battery charging jointly optimized without major trade-offs. The knee solutions are prioritized in SK-MOEA/D as they provide robust real-time operating strategies.

 doi:10.20944/preprints202603.2378.v1

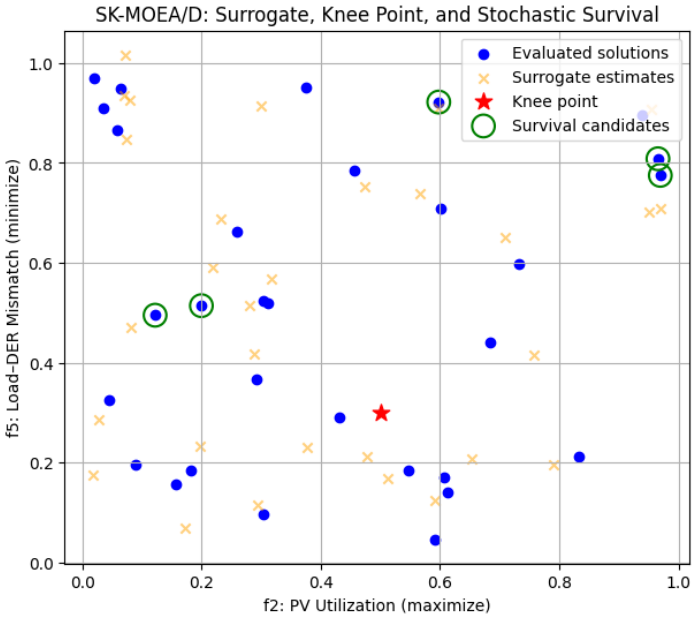

Figure 4. Operational schematic in terms of theoretical approach in the context of smart grid

Algorithm 5 Hybrid SK-MOEA/D Optimization Framework (Extended EMS Study)

Require: Population size N, reference directions Λ, generations G
Ensure: Pareto front approximation for $\{f_1', f_2', f_3', f_4'\}$
Load OPAL microgrid dataset (P_{PV}, P_{load}, SOC)
Initialize population $P = \{\mathbf{x}_1, \ldots, \mathbf{x}_N\}$ within decision bounds
Evaluate physical objectives $F(\mathbf{x}_i)$ for all $\mathbf{x}_i \in P$
Train surrogate models $\hat{f}_k(\mathbf{x})$ using Random Forest, $k \in \{1, 2, 3, 4\}$
for $g = 1$ to G **do**
    Predict objective values $\hat{F}(\mathbf{x})$ using surrogate models
    Generate offspring using MOEA/D variation operators
    Select subset of offspring for physical EMS evaluation
    Evaluate selected candidates using EMS simulation model
    Update surrogate models with newly evaluated data
    Identify knee solutions on current Pareto front
    Compute diversity measure among candidate solutions
    Apply stochastic survival selection using score

$$S(x) = -g(x) + \beta\kappa(x) + \delta D(x) - \alpha U(x)$$

    Replace dominated individuals emphasizing knee preference and diversity
end for
Extract final non-dominated solution set P^*
Compute EMO performance metrics (IGD, Hypervolume, Spread)
Perform statistical evaluation across runs (Wilcoxon, Friedman tests)
Select final EMS dispatch using knee-point decision strategy
return P^*

Stochastic-Elitist Survival

To maintain a balance between convergence and diversity, the survival of each solution is determined probabilistically based on a composite score that integrates scalarized fitness, knee preference, diversity, and surrogate uncertainty [12]:

$$S(x) = -g_n(x) + \beta\kappa_n(x) + \delta D_n(x) - \alpha U_n(x) \tag{25}$$

$$p_i^{(\text{surv})} = \frac{\exp(S(x_i)/\tau)}{\sum_j \exp(S(x_j)/\tau)} \tag{26}$$

 doi:10.20944/preprints202603.2378.v1

where $g_n(x)$ denotes the normalized scalarized MOEA/D fitness, $\kappa_n(x)$ represents the normalized knee preference score, $D_n(x)$ is the normalized diversity measure, and $U_n(x)$ corresponds to the normalized surrogate uncertainty. The parameter τ controls the stochastic selection temperature, while α, β, and δ balance uncertainty penalization, knee prioritization, and diversity preservation, respectively.

Knee Point Detection and Prioritization

A real-time knee point detection method [37,48–50] is also incorporated to identify solutions that provide optimal trade-offs, which is particularly valuable in practical decision-making scenarios. In Sections A and B, knee points (KP) are identified using distance-based compromise criteria, while in Section C, a score-based knee preference is incorporated within the stochastic survival mechanism.

$$KP(x) = CompromiseScore(\tilde{F}(x)) \tag{27}$$

where $\tilde{F}(x)$ denotes the normalized objective vector. The function CompromiseScore evaluates the trade-off characteristics in normalized objective space, assigning higher values to solutions that represent strong compromise regions among conflicting objectives.

Surrogate Model

The surrogate layer reduces expensive evaluations by learning an approximate mapping between decision vectors and objective values [47,51]. For real-world energy system applications, the estimation of efficient solutions is critical. To address the challenge of expensive evaluations, a surrogate model [52,53] is utilized. This method supports the evaluation of battery and OPAL power sharing, as well as power mismatch. It uses real-time microgrid data to quickly train the surrogate model during optimization. The system chooses between true and surrogate evaluations based on the degree of variation in the system [54,55]. The models used in this work were trained and validated using a data-driven approach to ensure reliable prediction of EMS objectives. The available dataset obtained from physical EMS evaluation was divided into 80% for model training and 20% reserved for independent testing.

For the assessment of model robustness, k-fold cross-validation (k=5) was applied on the training set, ensuring that the models generalize across different data partitions. Model performance was evaluated using standard regression metrics mentioned in table 6. For the GP model, predictive uncertainty $\sigma(x)$ was also obtained (equation 37), allowing the analysis of uncertainty error relationships. The correlation between prediction error and uncertainty is evaluated to verify whether higher uncertainty corresponds to larger prediction errors, supporting reliable surrogate-assisted selection. Moreover, the surrogate models were trained only on previously evaluated solutions, while newly generated candidate solutions were predicted and and selectively validated through physical replay.

$$\min_{\theta} \sum_{i=1}^{N} \left(\hat{f}(x_i;\theta) - f(x_i) \right)^2, \tag{28}$$

where θ represents surrogate parameters and $\hat{f}$ is the model prediction. This formulation represents a generic supervised regression objective; in the implementation, surrogate learning is performed using Random Forest regression. The uncertainty of the population is monitored using entropy Where p_i represents a probability related to normalized diversity. Entropy-based variation can be used as a diversity monitoring indicator; however, the reported experiments employ a fixed termination criterion of $G_{\max} = 120$ generations.

$$H = -\sum_{i=1}^{n} p_i \log(p_i), \tag{29}$$

 doi:10.20944/preprints202603.2378.v1

5. Results and Discussion

5.1. Section A Results (Physical validation)

To demonstrate the result of the grid-forming system a comparison table (4, 5) has been formulated where it shows the important factors of the optimization process. In the table the actual dispatch power from each components such as *PV_sup_W*, *Batt_sup_W*, *OPAL_sup_W*, *Curt_W* are also listed. The total power supply (*Total_sup_W*) is also represents the total (Net total power generation) contributions from DERs including MG (OPAL) to the Smart Grid system.

The operating level of the battery also calculated from the optimization process and included in the each tables as *SOC%*. From table 5, it can be seen that MOEA/D achieves the PV generation around 1181.2 W which tell us the PV usage was contributed more among the total energy requirement. It also showed the curtailed PV, indicating that the available PV was higher but was curtailed to balance the system. Then mismatch was also logged by using the absolute difference between supply and demand. The renewable fraction % was computed as $\frac{P_{\text{PV,used}}}{P_{\text{load}}} \times 100$, indicating the percentage of demand met by PV generation.

Table 4. Run-level statistical summary for Section A over 20 independent runs

Algorithm	HV	Spacing	Knee Dist.	Pareto Size	Knee Mismatch (W)
MOEA/D	0.8091 ± 0.0051	0.9836 ± 0.0667	0.7276 ± 0.0767	117.95 ± 0.76	27.54 ± 48.18
Smart-Seed MOEA/D	0.8068 ± 0.0050	1.0080 ± 0.0401	0.6965 ± 0.0047	118.15 ± 0.81	13.53 ± 7.20
Knee-Guided MOEA/D	0.8096 ± 0.0029	1.0047 ± 0.0558	0.7159 ± 0.0656	117.45 ± 0.89	24.07 ± 40.13

Table 5. Run-wise operational performance of Knee-Guided MOEA/D across 20 independent runs (Section A). The representative median-HV run is highlighted in bold, and degraded runs are shown in italic.

Seed	f_1	f_2	f_3	f_5	PV sup (W)	Batt sup (W)	OPAL sup (W)	Curt (W)	SOC (%)	Total sup (W)	Mismatch (W)	Renew. (%)	Load Cov. (%)
0	0.817	0.085	0.085	0.007	1098.6	47.1	45.7	356.8	79.9	1191.3	8.66	91.55	99.28
1	0.818	0.084	0.084	0.007	1099.4	51.1	41.1	222.6	57.6	1191.6	8.44	91.61	99.30
2	0.824	0.062	0.063	0.004	1125.8	15.8	53.7	310.1	47.0	1195.4	4.64	93.82	99.61
3	0.826	0.051	0.052	0.003	1138.9	53.7	4.22	180.7	97.7	1196.8	3.20	94.91	99.73
4	0.830	0.021	0.027	0.001	1174.2	2.08	23.0	267.0	69.5	1199.3	0.71	97.85	99.94
5	0.817	0.089	0.086	0.008	1093.3	23.8	73.7	405.3	77.4	1190.8	9.23	91.11	99.23
6	*0.629*	*0.335*	*0.330*	*0.110*	*798.4*	*65.1*	*204.1*	*699.3*	*100.0*	*1067.6*	*132.4*	*66.53*	*88.97*
7	**0.811**	**0.104**	**0.105**	**0.011**	**1074.8**	**45.6**	**66.5**	**103.6**	**58.3**	**1186.9**	**13.15**	**89.57**	**98.90**
8	0.810	0.105	0.107	0.011	1073.6	35.6	77.3	424.7	65.2	1186.5	13.53	89.47	98.87
9	0.803	0.123	0.122	0.015	1052.9	119.2	9.94	36.0	63.8	1182.1	17.92	87.75	98.51
10	0.829	0.026	0.031	0.001	1168.7	29.5	0.88	266.6	46.4	1199.0	0.98	97.39	99.92
11	0.815	0.091	0.096	0.009	1090.6	93.1	5.81	4.80	61.5	1189.5	10.52	90.88	99.12
12	0.830	0.016	0.016	0.000	1181.2	14.1	4.35	176.0	55.0	1199.7	0.31	98.43	99.97
13	0.815	0.095	0.091	0.009	1085.8	75.6	28.2	310.5	47.2	1189.7	10.34	90.48	99.14
14	*0.599*	*0.358*	*0.353*	*0.126*	*769.9*	*264.2*	*14.2*	*353.6*	*64.4*	*1048.4*	*151.6*	*64.16*	*87.36*
15	0.819	0.079	0.080	0.006	1104.9	66.5	21.0	375.1	71.1	1192.4	7.59	92.08	99.37
16	0.826	0.052	0.050	0.003	1137.8	0.24	58.9	327.0	54.4	1196.9	3.09	94.82	99.74
17	*0.630*	*0.330*	*0.331*	*0.109*	*803.9*	*248.3*	*16.5*	*502.2*	*56.8*	*1068.7*	*131.3*	*66.99*	*89.06*
18	0.807	0.115	0.114	0.013	1062.1	0.14	122.1	332.5	90.7	1184.3	15.70	88.51	98.69
19	0.819	0.075	0.084	0.006	1109.7	58.3	24.4	371.2	91.1	1192.4	7.60	92.48	99.37

The load coverage has been indicated by fraction of the load being met. In terms of computational aspect the crowding distance (equation 30) has been calculated in objective space for an approximate diversity measure where higher value indicates the better diversity on the pareto front [41,56,57]. It also shows how well solutions are distributed across trade-offs. The HV value indicates the pareto front coverage to a baseline (MOEA/D) system to see the performance in quality measure of multi-objective aspect [58].

$$CD_i = \sum_{k=1}^{m} \frac{f_k(i+1) - f_k(i-1)}{f_k^{\max} - f_k^{\min}}. \tag{30}$$

The results presented in tables (4, 5) highlight several key performance characteristics of the proposed framework. From the result, the HV values (approximately 0.81 with low variance across seeds) indicate consistent convergence toward a high-quality Pareto front. In terms of physical perspective, one of the result showed a very low mismatch achieved by the knee solutions. In several

 doi:10.20944/preprints202603.2378.v1

runs, the mismatch was reduced to 1 W. This demonstrates that the proposed EMS formulation was achieving near supply-demand balance under realistic operating conditions.

In addition, the load coverage consistently exceeds 99%, indicating a highly reliable energy management strategy. At the same time, the renewable fraction reaches up to approximately 97%, showing that the optimization effectively prioritizes renewable energy utilization without compromising system stability. Also the large Pareto set size (approximately 118 solutions) further confirms that the algorithm maintains strong diversity and provides multiple viable operating points.

Finally, the results presented in figures 5 and 6 shows the Statistical comparison of MOEA/D, Smart-Seed MOEA/D, and the proposed Knee-Guided MOEA/D across 20 independent runs. It showed the HV values was within approximately 0.795–0.815, with the proposed method achieving a comparable median (0.81) and reduced variability. The knee mismatch was typically within 5–20 W; however it has been found that the baseline MOEA/D has the mismatch around ∼150 W. The Pareto size remains stable (116–119 solutions) across all methods, indicating that the improvements are achieved without compromising solution diversity.

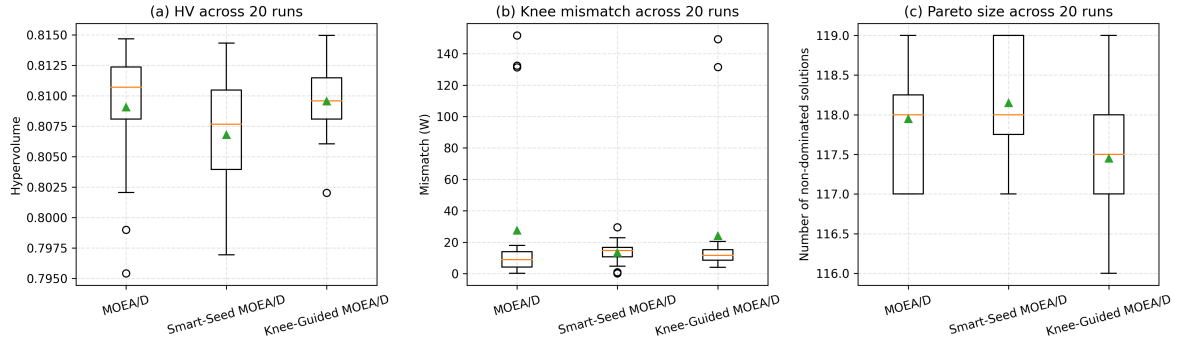

Figure 5. Statistical performance comparison across 20 runs (HV, knee mismatch, and Pareto size)

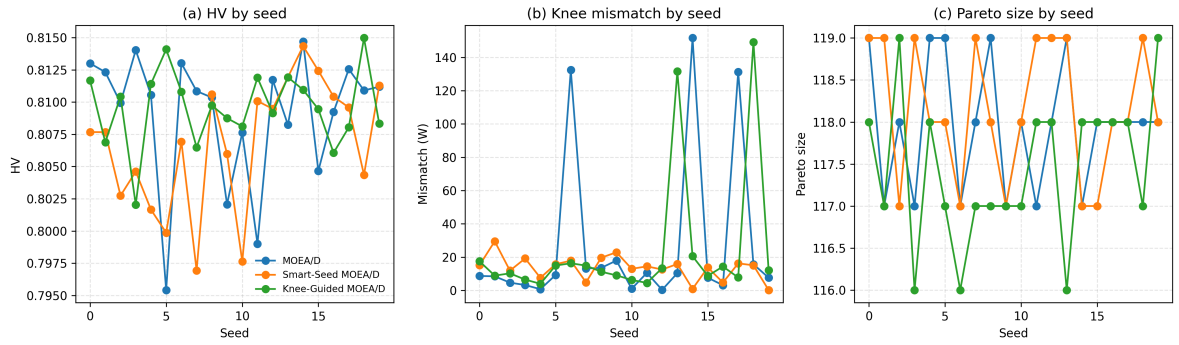

Figure 6. Per-seed performance analysis across 20 runs (HV, knee mismatch, and Pareto size)

In the per-seed performance analysis graph it can be seen that, the HV values are generally concentrated between 0.805 and 0.815, although baseline MOEA/D shows a decrease to ∼0.795, which were not observed in the proposed method. The mismatch plot reveals that most runs achieve 5–20 W, but baseline methods produce several extreme spikes exceeding 130–150 W, while the proposed approach reduces the occurrence of such sudden increase. The Pareto size remains nearly constant (117–119 solutions) across seeds, confirming consistent diversity across all algorithms.

5.2. Section B Results (Surrogate based Replay validation)

To validate the effectiveness, robustness, and computational efficiency of the data-driven MOEA/D optimizer for grid connected mode, a performance indicator equations (31)–(37) has been employed. These indicators originate from established EMO, Multi-Fidelity Optimization, and Smart-Grid control literature [59–64]. These metrics measured the convergence, diversity, and knee-behavior of the obtained Pareto set in the grid-connected optimization stage. As the algorithm optimizes

 doi:10.20944/preprints202603.2378.v1

multiple heterogeneous objectives, Pareto geometry is essential to determine whether the optimizer correctly captures trade-offs relevant for EMS operation or not.

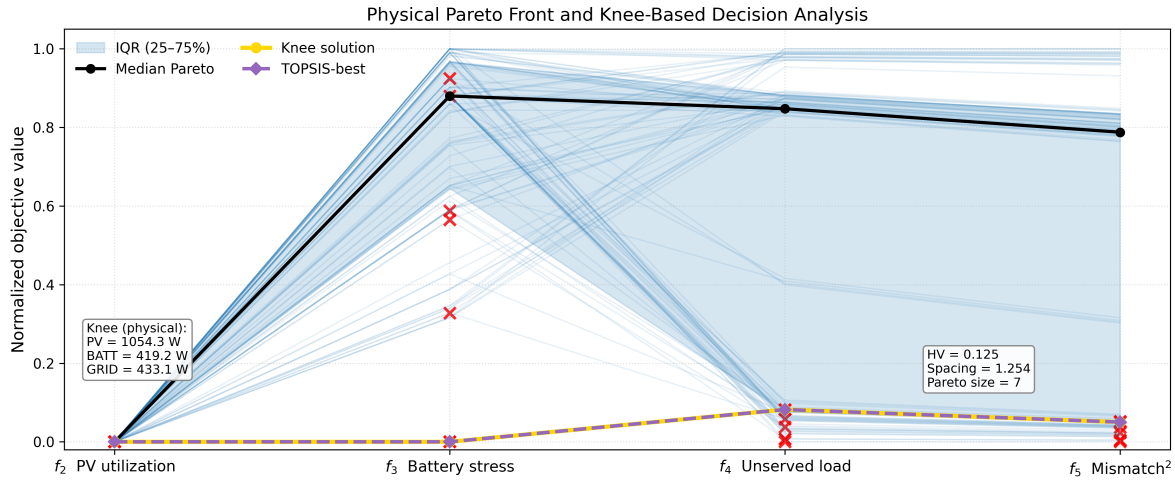

Figure 7. Surrogate–physical Pareto alignment and decision-space behavior of the hybrid EMS

To quantify the volume of the objective space dominating by the approximate Pareto set ($\mathcal{P}$) with respect to a reference point (z^{ref}) the HV indicator has been used, which indicates better convergence and spread. We have also runs the optimization measure to calculate the spacing which measures the uniformity of distribution of $\mathcal{P}$ whether a Lower spacing indicates well-distributed solutions across trade-offs. To measure the distance from the reference Pareto front ($\mathcal{P}^*$) to the obtained solutions, only the dominated component of IGD is included. A lower IGD$^+$ value indicates better convergence of the solutions.

Since the EMS optimization often prioritizes compromise between mismatch and battery degradation, knee solutions are particularly balancing this. A smaller $D_{\text{knee-dist}}$ indicates that a solution lies closer to the normalized ideal region and therefore represents a stronger compromise among the competing objectives. To see how well the surrogate model works for physical objectives and to check its reliability, we compare the surrogate predictions $\hat{f}_m(x)$ with the true objective values $f_m(x)$ using standard regression error and uncertainty measures.

The evaluation metrics such as MAE, RMSE, and uncertainty-error correlation listed, which shows how predictive uncertainty $\sigma_m(x)$ relates to the absolute prediction error $e_i = |f_m(x_i) - \hat{f}_m(x_i)|$ (equation 37). If there is a strong positive correlation, it means that uncertainty-based selection in the method is reliable. To check how often the true error in the EMS strategy is greater than the surrogate uncertainty, we report robust surrogate behavior metrics.

$$HV(\mathcal{P}) = \text{vol}\left(\bigcup_{x\in\mathcal{P}} [f_1(x), z_1^{\text{ref}}] \times \cdots \times [f_M(x), z_M^{\text{ref}}] \right). \tag{31}$$

$$IGD^+(\mathcal{P}, P^*) = \frac{1}{|P^*|} \sum_{y\in P^*} \min_{x\in\mathcal{P}} \sqrt{\sum_{m=1}^{M} (\max(0, f_m(x) - f_m(y)))^2}. \tag{32}$$

$$S = \sqrt{\frac{1}{N}\sum_{i=1}^{N} (d_i - \bar{d})^2}, \qquad d_i = \min_{j\neq i} \sum_{m=1}^{M} |f_m(x_i) - f_m(x_j)|. \tag{33}$$

$$D_{\text{knee-dist}} = \min_{x\in\mathcal{P}} \|\tilde{f}(x)\|_2, \qquad \tilde{f} = \frac{f - f^{\min}}{f^{\max} - f^{\min}}. \tag{34}$$

$$\text{MAE}_m = \frac{1}{N}\sum_{i=1}^{N} \left| f_m(x_i) - \hat{f}_m(x_i) \right|. \tag{35}$$

 doi:10.20944/preprints202603.2378.v1

$$\mathrm{RMSE}_m = \sqrt{\frac{1}{N}\sum_{i=1}^{N}\left(f_m(x_i) - \hat{f}_m(x_i)\right)^2}. \tag{36}$$

$$\rho_{\sigma,e} = \mathrm{Corr}(\sigma_m(x_i), |e_i|). \tag{37}$$

To show the effectiveness of the proposed algorithm, a generation-based plots were presented by figure 8. This plot illustrates generation-wise convergence behavior, and shows how the proposed surrogate-assisted EMO framework converges under the median PV/load scenario. Each row represents a selected generation and displays the normalized objective space [65], the physically evaluated Pareto front, and the identified knee solution.

Early in the optimization (Gen 6-18), surrogate-evaluated solutions (green crosses) are spread out, in both objective space and decision space (f_5) covering nearly the full range up to 1.0. In addition, physically evaluated solutions cluster near $f_5 \approx 0$, showing that feasibility is mainly enforced by physically replaying top candidates. At this stage, the knee point is close to the origin, indicating a constraint-dominated regime in which only low-mismatch solutions are non-dominated.

At generations 18 to 30, the surrogate model gradually learns the trade-off structure of the EMS problem. During the middle generations (30 to 42), the surrogate guides the population to converge toward a feasible solution. At this stage, the surrogate population forms a tight cluster in decision space, especially around PV values of about 900 to 910 W and Battery values of about 452 to 454 W. This indicates that the surrogate has learned the structure of the feasible operating region, so MOEA/D can avoid infeasible or poor regions without needing costly feasible replay.

In later generations, surrogate and physically evaluated solutions closely match along a clear Pareto front. The normalized mismatch values for Pareto-optimal solutions remain near zero ($f_5 < 0.05$), while other objectives, like battery stress (f_3), stay within a steady range. After the knee point, improvements become minimal. The knee remains in the same position across generations, which shows that the optimization has converged. These results indicate that the surrogate-assisted EMO framework speeds up convergence and keeps the physical Pareto structure.

doi:10.20944/preprints202603.2378.v1

Table 6. Integrated evaluation summary of the surrogate-assisted MOEA/D framework in Section B

Category	Metric	Value	Interpretation
Surrogate model validation			
	f_3 battery stress (R^2)	1.0000	High accuracy due to smooth and structured battery energy behavior
	f_4 unserved ratio (R^2)	0.8839	Moderate accuracy because it captures only unserved energy with simpler dynamics
	f_5 mismatch^2 (R^2)	0.4398	Lower accuracy due to nonlinear squared mismatch effects
	Uncertainty coverage (PIC95)	0.8747–1.0000	High reliability of prediction intervals
	Hybrid TOPSIS/knee consistency	TOPSIS index = knee index = 29	Decision ranking remained consistent
Run-level EMO performance over 20 runs			
	Population size	120	Consistent parameter setting across runs
	Replay size	$\approx$ 110–116	Large replay subset physically validated
	Hypervolume	0.1271 ± 0.0334	Stable but compact feasible Pareto region
	Spacing	1.0298 ± 0.2955	Moderate spread under constrained replay conditions
	Pareto size	6.10 ± 1.59	Limited feasible diversity in grid-following mode
	Crowding mean	1.329	Balanced solution distribution across objectives
	Entropy	1.550	Acceptable diversity in objective space
	Knee mismatch^2	466196.18 ± 128463.76	High residual mismatch under high-load conditions
	Knee unserved load	676.46 ± 95.12 W	Feasible solutions remain support-dominated
Representative decision quality			
	Representative seed	14	Median-HV run selected for interpretation
	TOPSIS score	0.9057	High closeness to the ideal physical trade-off
	Knee load coverage	$\approx$ 46–49%	Partial supply under constrained operating conditions
	Knee renewable fraction	0%	PV contribution remained negligible in replay-selected points
	Knee battery dispatch	$\approx$ 419–498 W	Battery support dominated feasible operation
	Knee grid support	$\approx$ 334–464 W	External support remained necessary
Diagnostic interpretation			
	Grid-following scenario behavior	Battery/grid dominated	Measured data favored conservative support-heavy decisions
	Renewable utilization	Limited	Low PV availability reduced direct renewable contribution
	Baseline comparison	Competitive but not superior	Section B is best interpreted as replay-guided decision support

 doi:10.20944/preprints202603.2378.v1

(a) In grid-connected mode, we applied a physical constraints via a replay stage which ensures that, if the surrogate model produces solutions that do not satisfy physical constraints such as power balance or device limits, each candidate solution is re-evaluated using the original system equations, and only feasible solutions are selected. In Section A, all solutions were evaluated directly on the PHIL system, ensuring feasibility. In Section C, all constraints are explicitly included in the optimization model, so no separate replay step is required. This ensures that only physically valid operating points are considered in the final decision.

(b) We have simulated over 5,000 real-time data points and set the population size using Das-Dennis reference directions (H=7, M=4). The results (table 6) indicate that, although the surrogate-assisted framework provides stable optimization behavior, the grid-following scenario is inherently constrained by limited renewable availability and high demand levels, leading to saturated operating points dominated by battery and grid support. The unserved-load value is reported in watts for physical interpretation, whereas the mismatch objective is squared to penalize large deficits more strongly; for EMO evaluation, the objectives are normalized so that scale differences do not dominate the comparison (table 6). The relatively high errors in PV utilization (MAE $= 1.0821$, RMSE $= 10.4185$) are attributed to near-zero PV activity and low signal variance, which inflate error metrics, whereas the surrogate maintains high accuracy for battery stress ($R^2 = 1.000$) and strong performance for unserved load ($R^2 = 0.8839$) supported by high uncertainty coverage (PIC95 up to 1.000).

(c) The high-fidelity physical replay used to validate surrogate decisions identified 7 physically non-dominating solutions. Multi-criteria ranking with TOPSIS also supports decision stability, as the knee solution scored 0.926, confirming its robustness across different decision-making methods. The 4D trade-off plot (figure 7) showed all physical Pareto solutions by blue transparent lines, where IQR is 25–75% per objective and the median Pareto trajectory is represented by a black line. The knee solution is marked with a gold line and markers, and physically replayed non-dominated solutions are marked in red.

(d) To maintain balance among objectives, normalization is applied during optimization, while physical values are preserved for analysis and interpretation [65]. The knee solutions lies inside the IQR, showing a Physical realism as PV utilization (f_2) remains near zero for most feasible solutions, indicating negligible renewable contribution under the given grid-following conditions. In contrast, battery stress (f_3) is relatively high (close to 0.9 in normalized space), confirming that battery dispatch is the dominant control action. The objectives f_4 (unserved load) and f_5 (mismatch^2) exhibit wider spread, as shown by the large interquartile region, reflecting variability in feasible supply-demand balancing. The knee solution (yellow) and TOPSIS-best solution [66] (purple) overlap closely, indicating strong agreement between geometric and decision-based selection criteria. The reported EMO indicators (HV = 0.125, spacing = 1.254, Pareto size = 7) confirm that the feasible Pareto set is compact but stable, which is expected under strict physical and operational constraints.

(e) In accordance with the EMO framework, the result found the convergence (HV $= 0.1271 \pm 0.0334$) with balanced diversity, followed by the crowding distance mean (1.329) and entropy (1.550). The relatively low HV value occurred because of the constrained feasible region in the grid-connected scenario. The TOPSIS-selected solution (index = 29, score $= 0.9057$) was relatively near the knee point, confirming decision validity. Operationally, the results indicate where battery ($\approx$ 419–498 W) and grid ($\approx$ 334–464 W) contributions prioritize for limited renewable utilization, while maintaining feasible load coverage ($\approx$ 46–49%). Overall, the results showed the framework as an EMS-based surrogate-assisted decision-support tool under constrained grid-following conditions.

 doi:10.20944/preprints202603.2378.v1

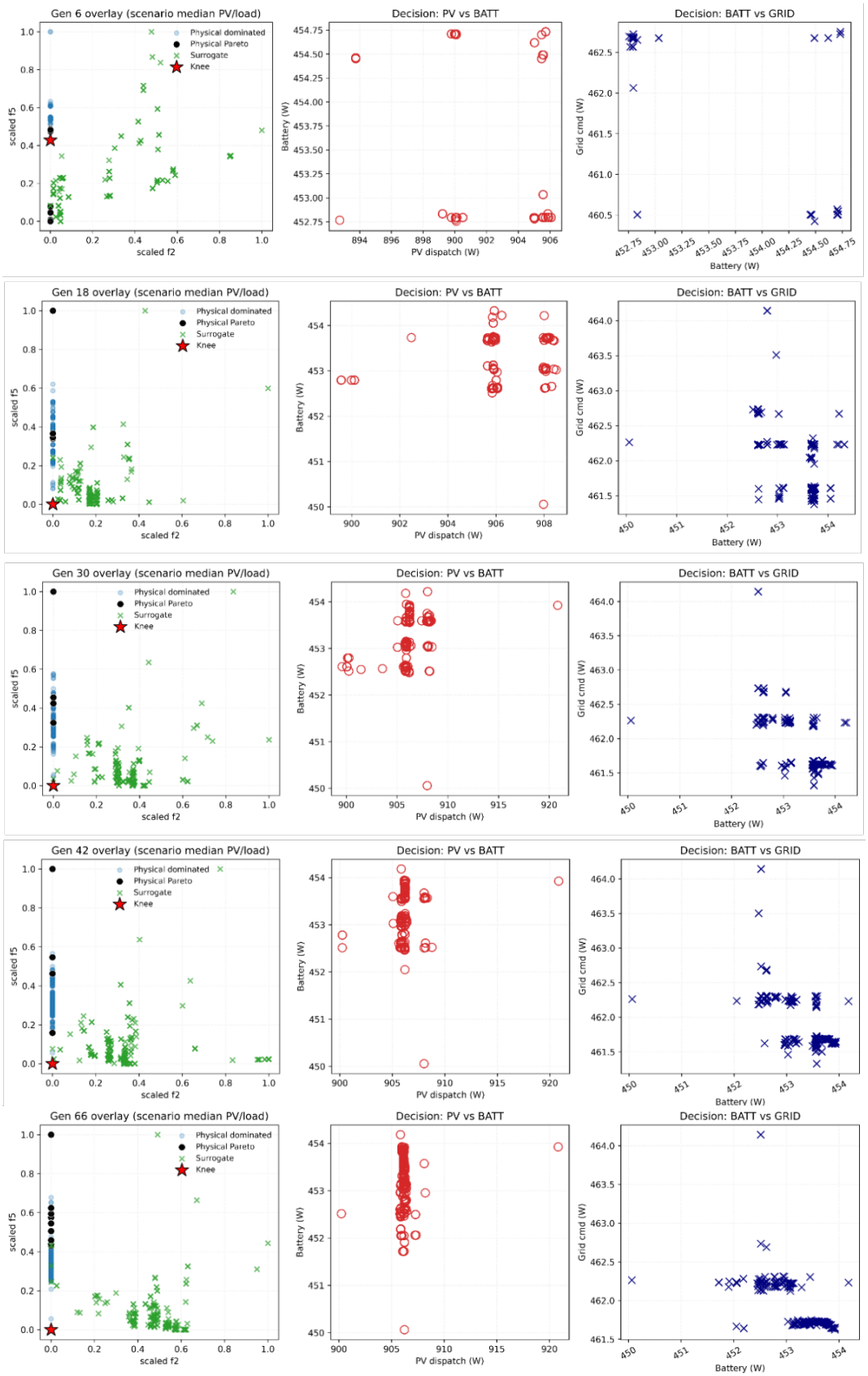

Figure 8. Convergence behavior of the surrogate-assisted EMO framework across generations

 doi:10.20944/preprints202603.2378.v1

5.3. Section C Results (Statistical EMO analysis)

In this section, the framework was extended with stochastic survival and Random-Forest-assisted surrogate modeling to evaluate additional objectives including economic cost, battery degradation, and reliability. The inclusion of stochastic selection enabled broader exploration of the solution space while maintaining feasible EMS operation under extended objective definitions.

Table 7. Representative knee solution characteristics for each algorithm (median-performance run).

Algorithm	Seed	RMSE (kW) ↓	Cost (€/kWh) ↓	Battery (EFC/year) ↓	LPSP ↓
Standard MOEA/D	14	0.0549	-0.0867	115.17	0.0684
Smart-Seed MOEA/D	14	**0.0554**	**-1.0264**	**0.30**	**0.0679**
SK-MOEA/D	14	1.3285	1.0779	102.11	3.1098

The SK-MOEA/D variant employs a RF surrogate model with 60 trees. The fraction of true evaluations was set to 0.30 and diversity injection to 0.10. The mutation standard deviation was 0.08 and the crossover probability was 0.90 (as defined in equation 25, 26 (formulated as $S(x) = -g(x) + \beta\kappa_n(x) + \delta D_n(x) - \alpha U_n(x)$)). In this formulation, $g(x)$ denotes the MOEA/D scalarized fitness function, $\kappa_n(x)$ represents the normalized knee preference indicator, $D_n(x)$ denotes the normalized diversity reward, and $U_n(x)$ corresponds to the normalized surrogate uncertainty penalty. The stochastic survival strategy with knee preference and diversity preservation consistent with the baseline framework while incorporating additional weighting parameters to control the influence of each component. The corresponding weights are α for the uncertainty penalty, β for the knee preference, and δ adjusts the diversity reward. The parameter τ controls the selection temperature in the stochastic survival mechanism. The operational constraints (equations 16-19) were defined using a power-balance tolerance of 100W, SOC limits of 40%-100%, and battery efficiency of 0.95 for both charging and discharging. The economic objective was formulated as a net operating cost per delivered energy using a grid import tariff of 0.22 €/kWh (approximate value used as current electricity price), an export tariff of 0.08 €/kWh, and a demand charge of 12 €/KW/month. The key findings from this section were as follows:

Table 8. Descriptive statistics of EMO performance metrics across 20 independent runs.

Metric	Algorithm	Mean	Std	Median	Q1	Q3	Min / Max
IGD	Standard MOEA/D	127.72	111.38	59.99	58.51	142.59	58.43 / 434.08
IGD	Smart-Seed MOEA/D	**58.43**	**0.02**	**58.43**	**58.42**	**58.44**	**58.41 / 58.46**
IGD	SK-MOEA/D	472.53	256.52	422.19	261.92	658.98	92.08 / 877.48
HV	Standard MOEA/D	136588	48981	145276	106118	171462	48580 / 218953
HV	Smart-Seed MOEA/D	**254604**	**11544**	**256131**	**245370**	**265808**	**235236 / 271102**
HV	SK-MOEA/D	156187	51653	158991	126839	194126	65560 / 250528
Spread	Standard MOEA/D	0.00644	0.00464	0.00511	0.00372	0.00938	0.00012 / 0.01627
Spread	Smart-Seed MOEA/D	0.00841	0.00348	0.00780	0.00644	0.01045	0.00232 / 0.01703
Spread	SK-MOEA/D	**0.01241**	**0.00528**	**0.01055**	**0.00935**	**0.01411**	**0.00617 / 0.02802**
ND	Standard MOEA/D	386.25	36.54	398	373.75	408.75	290 / 426
ND	Smart-Seed MOEA/D	**399.20**	**30.58**	**402**	**391.50**	**421.50**	**311 / 437**
ND	SK-MOEA/D	307.05	83.09	343	274.75	369.25	114 / 395
Runtime	Standard MOEA/D	301.87	390.09	206.17	179.06	240.23	147.70 / 1943.99
Runtime	Smart-Seed MOEA/D	**212.22**	**53.86**	**198.40**	**177.45**	**223.66**	**147.69 / 344.35**
Runtime	SK-MOEA/D	5529.87	7703.25	3365.48	1803.91	6692.99	1625.12 / 36359.60
TrueEvals	Standard MOEA/D	54600	0	54600	54600	54600	54600 / 54600
TrueEvals	Smart-Seed MOEA/D	54600	0	54600	54600	54600	54600 / 54600
TrueEvals	SK-MOEA/D	**16895**	**0**	**16895**	**16895**	**16895**	**16895 / 16895**

The key findings of this section summarized in table 7, 8, and 9. Where Smart-Seed MOEA/D achieves the stable EMO performance, with the lowest IGD (58.43) and highest HV (254604) value. In contrast, SK-MOEA/D reduces the number of true evaluations from 54,600 to 16,895 (approximately 69% reduction), demonstrating improved computational efficiency. This reduction is accompanied by lower IGD (equation 32) and HV values, reflecting a trade-off between optimization quality and evaluation cost. In addition, SK-MOEA/D produces a smaller Pareto set (307 vs 399) because of surrogate-assisted filtering and stochastic survival, indicating selective solution retention. The higher spread value (0.0124) suggests a broader exploration of the solution space.

 doi:10.20944/preprints202603.2378.v1

Table 9. Performance comparison and statistical significance analysis under identical settings (20 runs, 120 generations).

Algorithm	IGD ↓	HV ↑	Spread ↑	ND ↑	Runtime ↓	True evals ↓
Standard MOEA/D	127.72 ± 111.38	1.37×10^5	0.00644	386	301.87	54600
Smart-Seed MOEA/D	**58.43 ± 0.02**	$\mathbf{2.55}\times10^5$	0.00841	**399**	**212.22**	54600
SK-MOEA/D	472.53 ± 256.52	1.56×10^5	**0.01241**	307	5529.87	**16895**
Statistical Tests						
IGD (Wilcoxon)	$p \approx 1.9 \times 10^{-6}$					
HV (Wilcoxon)	$p \approx 1.9 \times 10^{-6}$					
Friedman Test	$p \approx 2.9 \times 10^{-7}$					

The statistical tests reveal significant differences. The Wilcoxon p-values for both IGD and HV were about $p = 1.9 \times 10^{-6}$, and the Friedman test p-value was about $p = 2.9 \times 10^{-7}$. These results suggest that the differences are unlikely to be due to random variation, while the surrogate model maintains stable predictive performance ($R^2 \approx 0.82$–0.90). The variability in decision outcomes was primarily influenced by stochastic survival and the sensitivity of knee-based selection, where it represents a compromise in the final solution. Therefore, the framework should be interpreted as a decision-oriented EMS optimization approach, where identifying feasible and balanced operating points is more relevant than maximizing Pareto front size or EMO metrics. The results confirm that surrogate-assisted stochastic optimization can significantly reduce evaluation cost while still enabling meaningful decision-making under highly conflicting EMS objectives.

6. Conclusion

In conclusion, this research presents a combined surrogate-assisted, knee-region preference, and stochastic survival based MOEA/D framework where stochastic survival supports the exploration of feasible solutions under extended objective settings. Although these methods have been studied separately in previous studies, we combined them and tested the approach with real microgrid and smartgrid operating data and technical objectives. The framework enables convergence to feasible solutions while revealing system limitations under different operating conditions. It provides a constraint-aware perspective on EMS operation rather than focusing on performance improvement. In section A, the HV values (≈ 0.809˜0.812) demonstrated a consistent optimization behaviour across 20 independent runs. The low knee mismatch values (10–15 W), stable Pareto sizes of approximately 117-118 solutions, indicate a reliable convergence and stable solution quality under controlled physical conditions.

In grid-following section, the framework revealed the impact of real-world operational constraints. The average HV value (0.127 ± 0.033) with a reduced Pareto size (6.10 ± 1.59) indicates a compact feasible region after physical replay filtering. The representative knee solution exhibited a mismatch of approximately 676.46 ± 95.12 W, with load coverage around 46–49% and negligible renewable contribution (0% PV utilization). The feasible operating points were primarily supported by battery dispatch (419–498 W) and grid support (334–464 W), reflecting constraint-driven system behaviour rather than algorithmic limitations.

Section C further expanded the framework by incorporating economic cost, battery degradation, and reliability objectives together with Random-Forest-assisted SK-MOEA/D optimization and statistical EMO evaluation. The results show that Smart-Seed MOEA/D achieved a stable convergence, while the proposed framework significantly reduced the number of physical evaluations. It maintained a stable Pareto diversity (Spread ≈ 0.0124).

Overall, this research provides a decision-based EMS optimization approach where a feasible operating point is automatically identified through knee-based selection from the Pareto set, without requiring explicit objective weighting. The knee solution represents a balanced compromise among conflicting technical, economic, and reliability objectives. The method reduces evaluation cost by limiting expensive real-system evaluations while preserving feasible, meaningful decisions. Therefore,

 doi:10.20944/preprints202603.2378.v1

the framework demonstrated that identifying feasible and balanced operating points is more relevant than maximizing Pareto front size or EMO metrics.

Future work will be focused on the enhancement of the robustness and consistency of the SK-MOEA/D framework under complex and more conflicting EMS scenarios, reducing evaluation cost and enabling practical decision-making. Because of multiple hardware components and the requirement for fast control command cycles, real-time dynamic deployment of the SK-MOEA/D framework is identified as an important extension and will be investigated in future work.

Acknowledgments

I would like to thank Christoph Steup, Group Leader in Swarm Technology at Fraunhofer IVI Dresden, for his valuable insights and guidance at the beginning of the project. His expert, experienced feedback was instrumental in advancing the project to the next stage.

I also thank Lab Engineers Jagadish Pyneni and Denis Niehusen from the School of Technology and Architecture (TEAC), SRH, as well as Technical Support Engineer Awab Baqr from OPAL-RT Technologies, for their assistance.

Declarations

The contributors to this research are the authors, and all data and supplementary documents are associated with the nicht-Drittmittel gefördertes Projekt at SRH University of Applied Sciences, Campus Berlin, Germany. Laboratory tests were conducted using the OPAL-RT power hardware-in-the-loop system and the Lucas Nülle photovoltaic, battery, and smart grid test bench.

(a) Funding : This research did not receive external funding.
(b) Consent for publication: All authors give their consent for publication.
(c) Data availability: The data supporting the findings of this study are available from the corresponding author upon reasonable request.
(d) Materials availability: All materials used in this study are available from the authors upon request.
(e) Code availability: The code developed for this work is available from the corresponding author upon reasonable request.
(f) Author contribution: All authors contributed to the study conception, methodology, analysis, and writing of the manuscript. All authors read and approved the final version.

Conflicts of Interest: The authors declare no conflict of interest.

References

1. Syahril M, R.M.A.; Ismail1, B. Microgrid synchronization using power offset through a central controller. In Proceedings of the Journal of Physics: Conference Series, 2019.
2. Shafiullah, M. Review of Recent Developments in Microgrid Energy Management Strategies. *Sustainability* **2022**, *14*, 14794. https://doi.org/10.3390/su142214794.
3. Venayagamoorthy, G.K.; Sharma, R.K.; Gautam, P.K.; Ahmadi, A. Dynamic Energy Management System for a Smart Microgrid. *IEEE Transactions on Neural Networks and Learning Systems* **2016**, *27*, 1643–1656. https://doi.org/10.1109/TNNLS.2016.2514358.
4. Aragües Peñalba, M.; Sumper, A. Special Issue on Microgrids. *Applied Sciences* **2019**, *9*, 4710. https://doi.org/10.3390/app9214710.
5. Vasilakis, A.; Zafeiratou, I.; Lagos, D.T.; Hatziargyriou, N.D. The Evolution of Research in Microgrids Control. *IEEE Open Access Journal of Power and Energy* **2020**, *7*, 331–343. https://doi.org/10.1109/OAJPE.2020.3030348.
6. Yazdani, A.; Iravani, R. *Voltage-Sourced Converters in Power Systems: Modeling, Control, and Applications*; John Wiley & Sons: Hoboken, NJ, USA, 2010.
7. Saiful Islam.; Sanaz Mostaghim.; Michael Hartmann. A Survey on Multi-Objective Optimization in Microgrid Systems. In Proceedings of the Proceedings of the IEEE Congress on Evolutionary Computation (CEC), Yokohama, Japan, 2024; pp. 1–8.

 doi:10.20944/preprints202603.2378.v1

8. Thirunavukkarasu, G.S.; Seyedmahmoudian, M.; Jamei, E.; Horan, B.; Mekhilef, S.; Stojcevski, A. Role of optimization techniques in microgrid energy management systems—A review. *Energy Strategy Reviews* **2022**, *43*, 100899. https://doi.org/10.1016/j.esr.2022.100899.
9. Sharma, S.; Kumar, V. A Comprehensive Review on Multi-objective Optimization Techniques: Past, Present and Future. *Archives of Computational Methods in Engineering* **2022**, *29*.
10. Deb, K. Multi-Objective Optimization Using Evolutionary Algorithms: An Introduction. In Proceedings of the Indian Institute of Technology Kanpur, PIN 208016, India, KanGAL Report Number 2011003, 2011.
11. Sengthavy Phommixay, Mamadou Lamine Doumbia, D.L.S. Review on the cost optimization of microgrids via particle swarm optimization. *International Journal of Energy and Environmental Engineering* **2020**.
12. Liu, S.; Yu, W.; Gao, W.; Lou, K.; Zhang, Y. Multi-objective optimization dispatch of PV-MG considering demand response actions. In Proceedings of the Proceedings of the 35th Chinese Control Conference (CCC), Chengdu, China, 2016.
13. Tian, Y.; Cheng, R.; Zhang, X.; Jin, Y. PlatEMO: A MATLAB Platform for Evolutionary Multi-Objective Optimization. In Proceedings of the Proceedings of the IEEE Congress on Evolutionary Computation (CEC), Donostia-San Sebastián, Spain, 2017; pp. 1–8.
14. Kalyanmoy Deb.; Amrit Pratap.; Sameer Agarwal.; T. Meyarivan. A Fast and Elitist Multiobjective Genetic Algorithm: NSGA-II. *IEEE Transactions on Evolutionary Computation* **2002**, *6*, 182–197. https://doi.org/10.1109/4235.996017.
15. Shabir, S.; Singla, R. A Comparative Study of Genetic Algorithm and Particle Swarm Optimization. *International Journal of Electrical Engineering* **2016**, *9*, 215–223.
16. Zhou, N.; Liu, N.; Zhang, J.; Lei, J. Multi-Objective Optimal Sizing for Battery Storage of PV-Based Microgrid with Demand Response. *Energies* **2016**, *9*, 591. https://doi.org/10.3390/en9080591.
17. Oulis Rousis, A.; Tzelepis, D.; Konstantelos, I.; Booth, C.; Strbac, G. Design of a Hybrid AC/DC Microgrid Using HOMER Pro: Case Study on an Islanded Residential Application. *Inventions* **2018**, *3*, 55. https://doi.org/10.3390/inventions3030055.
18. Saxena, V.; Kumar, N.; Nangia, U. Recent Trends in the Optimization of Renewable Distributed Generation: A Review. *Ingeniería e Investigación* **2022**, *42*, e97702. https://doi.org/10.15446/ing.investig.97702.
19. Ch. A. Nallolla.; M. M. Reddy.; G. S. Reddy. Multi-Objective Optimization Algorithms for a Hybrid AC/DC Microgrid Using RES: A Comprehensive Review. *Electronics* **2023**, *12*, 1062. https://doi.org/10.3390/electronics12041062.
20. Mark Kipngetich Kiptoo.; Oludamilare Bode Adewuyi.; Mohammed Elsayed Lotfy.; Tomonobu Senjyu.; Paras Mandal.; Mamdouh Abdel-Akher. Multi-Objective Optimal Capacity Planning for 100% Renewable Energy-Based Microgrid Incorporating Cost of Demand-Side Flexibility Management. *Applied Sciences* **2019**, *9*, 3855. https://doi.org/10.3390/app9183855.
21. Geng, S.; Wu, G.; Tan, C.e.a. Multi-Objective Optimization of a Microgrid Considering the Uncertainty of Supply and Demand. *Sustainability* **2021**.
22. Islam, Saiful.; Mostaghim, Sanaz.; Hartmann, Michael. Multi-Objective Optimization Algorithms for Energy Management Systems in Microgrids: A Control Strategy Based on a PHIL System **2025**. pp. 1–5. https://doi.org/10.1109/ISGTEurope64741.2025.11305355.
23. Kurundkar, K.M.; Karve, G.M.; Vaidya, G.A. Techno-Economic Analysis and Optimal Sizing of Stand-alone Hybrid AC–DC Microgrid by Nature-Inspired Firefly Algorithm and Particle Swarm Optimization. In Proceedings of the Proceedings of the 2021 International Conference on Intelligent Technologies (CONIT), Hubballi, India, 2021; pp. 1–6.
24. Saiful Islam.; Sanaz Mostaghim.; Michael Hartmann. Multi-Objective Optimization Algorithms for Energy Management System in Microgrids Including Control Strategy. In Proceedings of the IEEE Symposia on Computational Intelligence for Energy, Transport and Environmental Sustainability (CIETES Companion), 2025. https://doi.org/10.1109/CIETESCompanion65203.2025.11003308.
25. Liang Zhang.; Bo Pang.; Ruipeng Yi.; Pengyu Gai.; Chunqing Xin.; Longjie Yang.; Huaqiang Li. Multi-Objective Day-Ahead Optimal Scheduling of Isolated Microgrid Considering Flexibility. In Proceedings of the E3S Web of Conferences, 2018, Vol. 53. https://doi.org/10.1051/e3sconf/20185301024.
26. Yongyi Huang.; Hasan Masrur.; Ryuto Shigenobu.; Ashraf Mohamed Hemeida.; Alexey Mikhaylov.; Tomonobu Senjyu. A Comparative Design of a Campus Microgrid Considering a Multi-Scenario and Multi-Objective Approach. *Energies* **2021**, *14*, 2853. https://doi.org/https://doi.org/10.3390/en14112853.

 doi:10.20944/preprints202603.2378.v1

27. Xiaomin Wu.; Weihua Cao.; Dianhong Wang.; Min Ding. Multi-objective Optimization Based on SPEA for the Microgrid Energy Dispatch. In Proceedings of the Proceedings of the 37th Chinese Control Conference, 2018. https://doi.org/https://doi.org/10.23919/ChiCC.2018.8483695.
28. Kalyanmoy Deb.; Himanshu Jain. An Evolutionary Many-Objective Optimization Algorithm Using Reference-Point-Based Nondominated Sorting Approach, Part I: Solving Problems With Box Constraints. *IEEE Transactions on Evolutionary Computation* **2014**, *18*, 577–601. https://doi.org/10.1109/TEVC.2013.2281535.
29. Lasseter, R.H.; Chen, Z.; Pattabiraman, D. Grid-Forming Inverters: A Critical Asset for the Power Grid. *IEEE Journal of Emerging and Selected Topics in Power Electronics* **2020**, *8*, 925–935. https://doi.org/10.1109/JESTPE.2019.2959271.
30. Lucas-Nülle. ESG 1 Smart Grid Trainer for Power Engineering, Smart Grid, and Microgrid Applications. https://www.lucas-nuelle.us/2768/apg/13582/ESG-1-Smart-Grid-Trainer.htm, 2025. [Online; accessed 23-April-2025].
31. Faa-Jeng Lin.; Chao-Fu Chang.; Yu-Cheng Huang.; Tzu-Ming Su. A Deep Reinforcement Learning Method for Economic Power Dispatch of Microgrid in OPAL-RT Environment. *Technologies* **2023**, *11*, 96. https://doi.org/10.3390/technologies11040096.
32. Sandro Kellermüller.; Artjoms Obushevs.; Miguel Ramirez Gonzalez.; Petr Korba. Digital Twin Development of a Dynamic Hardware Emulator. *Energies* **2022**, *15*, 4547. https://doi.org/10.3390/en15134547.
33. OPAL-RT Technologies. OP1400 Series 4-Quadrant PHIL Amplifier. https://www.opal-rt.com/op1400-4-quadrant-power-amplifier/, 2025. [Online; accessed 23-April-2025].
34. Boris Djartov.; Sanaz Mostaghim. Multi-objective Multiplexer Decision Making Benchmark Problem. In Proceedings of the Proceedings of the Companion Conference on Genetic and Evolutionary Computation (GECCO '23 Companion), 2023, pp. 1676–1683. https://doi.org/10.1145/3583133.3596360.
35. Tobias Benecke.; Sanaz Mostaghim. Effects of Optimal Genetic Material in the Initial Population of Evolutionary Algorithms. In Proceedings of the 2023 IEEE Symposium Series on Computational Intelligence (SSCI), 2023, pp. 1386–1391. https://doi.org/10.1109/SSCI52147.2023.10372037.
36. Andre Opris. A First Runtime Analysis of NSGA-III on a Many-Objective Multimodal Problem: Provable Exponential Speedup via Stochastic Population Update, 2025, [arXiv:cs.NE/2505.01256].
37. Jürgen Branke.; Kalyanmoy Deb.; Henning Dierolf.; Matthias Osswald. Finding Knees in Multi-objective Optimization. In Proceedings of the Parallel Problem Solving from Nature – PPSN VIII, 2004, Vol. 3242, *Lecture Notes in Computer Science*, pp. 722–731. https://doi.org/10.1007/978-3-540-30217-9_73.
38. Junfeng Tang.; Handing Wang.; Lin Xiong. Surrogate-assisted multi-objective optimization via knee-oriented Pareto front estimation. *Swarm and Evolutionary Computation* **2023**, *77*, 101252. https://doi.org/10.1016/j.swevo.2023.101252.
39. Saiful Islam.; Sanaz Mostaghim.; Michael Hartmann. Multi-Objective Optimization Algorithms for Energy Management Systems in Microgrids: A Control Strategy Based on a PHIL System, 2025, [arXiv:eess.SY/2505.18210].
40. Rui Wang.; Jian Xiong.; Hisao Ishibuchi.; Guohua Wu.; Tao Zhang. On the effect of reference point in MOEA/D for multi-objective optimization. *Applied Soft Computing* **2017**, *58*, 25–34. https://doi.org/10.1016/j.asoc.2017.04.002.
41. Qingfu Zhang.; Hui Li. MOEA/D: A Multiobjective Evolutionary Algorithm Based on Decomposition. *IEEE Transactions on Evolutionary Computation* **2007**, *11*, 712–731. https://doi.org/10.1109/TEVC.2007.892759.
42. Kalyanmoy Deb.; Ram Bhushan Agrawal. Simulated Binary Crossover for Continuous Search Space. *Complex Systems* **1995**, *9*, 115–148.
43. Kalyanmoy Deb. *Multi-Objective Optimization Using Evolutionary Algorithms*; John Wiley & Sons: Chichester, UK, 2001.
44. Kalyanmoy Deb. An efficient constraint handling method for genetic algorithms. *Computer Methods in Applied Mechanics and Engineering* **2000**, *186*, 311–338. https://doi.org/10.1016/S0045-7825(99)00389-8.
45. Daniel Molina.; Antonio LaTorre.; Francisco Herrera. An Insight into Bio-inspired and Evolutionary Algorithms for Global Optimization: Review, Analysis, and Lessons Learnt over a Decade of Competitions. *Cognitive Computation* **2018**. https://doi.org/10.1007/s12559-018-9554-0.
46. Nery Riquelme.; Christian von Lücken.; Benjamín Barán. Performance metrics in multi-objective optimization. In Proceedings of the 2015 Latin American Computing Conference (CLEI 2015), 2015, pp. 1–11. https://doi.org/10.1109/CLEI.2015.7360024.
47. Yaochu Jin. Surrogate-assisted evolutionary computation: Recent advances and future challenges. *Swarm and Evolutionary Computation* **2011**. https://doi.org/10.1016/j.swevo.2011.05.001.

 doi:10.20944/preprints202603.2378.v1

48. Cristian Ramírez-Atencia.; Sanaz Mostaghim.; David Camacho. AsKPNSGA-II: Knee Point Based MOEA with Self-Adaptive Angle for Mission Planning Problems, 2020, [2002.08867].
49. Lily Rachmawati.; Dipti Srinivasan. Multiobjective Evolutionary Algorithm With Controllable Focus on the Knees of the Pareto Front. *IEEE Transactions on Evolutionary Computation* **2009**, *13*, 810–824. https://doi.org/10.1109/TEVC.2009.2017515.
50. Xingyi Zhang.; Ye Tian.; Yaochu Jin. A Knee Point-Driven Evolutionary Algorithm for Many-Objective Optimization. *IEEE Transactions on Evolutionary Computation* **2015**, *19*, 761–776. https://doi.org/10.1109/TEVC.2014.2378512.
51. Qingfu Zhang.; Wudong Liu.; Edward Tsang.; Botond Virginas. Expensive Multiobjective Optimization by MOEA/D With Gaussian Process Model. *IEEE Transactions on Evolutionary Computation* **2010**, *14*, 456–474. https://doi.org/10.1109/TEVC.2009.2033671.
52. Deb, Kalyanmoy, P.C.R.; m, R. Surrogate Modeling Approaches for Multiobjective Optimization: Methods, Taxonomy, and Results. 2021, Vol. 26. https://doi.org/10.3390/mca26010005.
53. Wei Gong.; Qingyun Duan.; Jianduo Li.; Chen Wang.; Zhenhua Di.; Aizhong Ye.; Chiyuan Miao.; Yongjiu Dai. Multiobjective adaptive surrogate modeling-based optimization for parameter estimation of large, complex geophysical models. *Water Resources Research* **2015**, *52*, 1982–2003. https://doi.org/10.1002/2015WR018230.
54. Michael T. M. Emmerich.; André H. Deutz. A Tutorial on Multiobjective Optimization: Fundamentals and Evolutionary Methods. *Natural Computing* **2018**, *17*, 585–609. https://doi.org/10.1007/s11047-018-9685-y.
55. Joshua D. Knowles. ParEGO: a hybrid algorithm with on-line landscape approximation for expensive multiobjective optimization problems. *IEEE Transactions on Evolutionary Computation* **2006**, *10*, 50–66. https://doi.org/10.1109/TEVC.2005.851274.
56. Hui Li.; Qingfu Zhang. Multiobjective optimization problems with complicated Pareto sets: MOEA/D and NSGA-II. *IEEE Transactions on Evolutionary Computation* **2009**, *13*, 284–302. https://doi.org/10.1109/TEVC.2008.925798.
57. Deb, K.; Pratap, A.; Agarwal, S.; Meyarivan, T. A fast and elitist multiobjective genetic algorithm: NSGA-II. *IEEE Transactions on Evolutionary Computation* **2002**. https://doi.org/10.1109/4235.996017.
58. Eckart Zitzler.; Lothar Thiele. Multiobjective Optimization Using Evolutionary Algorithms: A Comparative Case Study **1998**. https://doi.org/10.1007/BFb0056872.
59. Zitzler, E.; Thiele, L.; Laumanns, M.; Fonseca, C.; da Fonseca, V. Performance assessment of multiobjective optimizers: an analysis and review. *IEEE Transactions on Evolutionary Computation* **2003**, *7*, 117–132. https://doi.org/10.1109/TEVC.2003.810758.
60. Hisao Ishibuchi.; Naoya Akedo.; Yusuke Nojima. Behavior of Multiobjective Evolutionary Algorithms on Many-Objective Knapsack Problems. *IEEE Transactions on Evolutionary Computation* **2015**, *19*. https://doi.org/10.1109/TEVC.2014.2315442.
61. David A. Van Veldhuizen.; Gary B. Lamont. Multiobjective Evolutionary Algorithms: Analyzing the State-of-the-Art. *Evol. Comput.* **2000**, *8*, 125–147. https://doi.org/10.1162/106365600568158.
62. Dimo Brockhoff.; Eckart Zitzler. Are All Objectives Necessary? On Dimensionality Reduction in Evolutionary Multiobjective Optimization **2006**. pp. 533–542.
63. Xingyi Zhang.; Ye Tian.; Yaochu Jin. A Knee Point-Driven Evolutionary Algorithm for Many-Objective Optimization. *IEEE Transactions on Evolutionary Computation* **2015**, *19*, 761–776. https://doi.org/10.1109/TEVC.2014.2378512.
64. Ryoji Tanabe.; Ke Li. Quality Indicators for Preference-Based Evolutionary Multiobjective Optimization Using a Reference Point: A Review and Analysis. *IEEE Transactions on Evolutionary Computation* **2024**, *28*, 1575–1589. https://doi.org/10.1109/tevc.2023.3319009.
65. He, L.; Ishibuchi, H.; Trivedi, A.; Wang, H.; Nan, Y.; Srinivasan, D. A Survey of Normalization Methods in Multiobjective Evolutionary Algorithms. *IEEE Transactions on Evolutionary Computation* **2021**, *25*, 1028–1048. https://doi.org/10.1109/TEVC.2021.3076514.
66. Dheda, D.; Albertyn, J.; Adetunji, K.; Liu, Z.; Abu-Mahfouz, A.M.; Cheng, L. Techno-Economic, Environmental, and Social Multi-Objective Optimization of a Grid-Connected Hybrid Renewable Energy System Using Metaheuristic Algorithms. *IEEE Access* **2025**, *PP*, 1–1. https://doi.org/10.1109/ACCESS.2025.3612294.